High-contrast sub-Doppler absorption spikes in a hot atomic vapor cell exposed to a dual-frequency laser field

Moustafa Abdel Hafiz, Denis Brazhnikov, Grégoire Coget, Alexei
Taichenachev, Valeriy Yudin, Emeric de Clercq, Rodolphe Boudot

High-contrast sub-Doppler absorption spikes in a hot atomic vapor cell exposed to a dual-frequency laser field

You may also be interested in:

Multi-photon resonance phenomena using Laguerre–Gaussian beams
Seyedeh Hamideh Kazemi and Mohammad Mahmoudi

Revisiting the four-level inverted-Y system under both Doppler free and Doppler broadened condition: an analytical approach
Arindam Ghosh, Khairul Islam, Dipankar Bhattacharyya et al.

Electromagnetictrapping of cold atoms
V I Balykin, V G Minogin and V S Letokhov

Observation of coherent effects using a mode-locked Rubidium laser
Aihua Zhang, Vladimir A Sautenkov, Yuri V Rostovtsev et al.

Laser cooling of atoms: a review
V S Letokhov, M A Ol'shanii and Yu B Ovchinnikov

Coherent population trapping in quantum systems
B D Agap'ev, M B Gorny, B G Matisov et al.

Coherent effects on the Zeeman sublevels of Rb
G Alzetta, S Cartaleva, Y Dancheva et al.

Experimental and theoretical comparison of different optical excitation schemes for a compact coherent population trapping Rb vapor clock
Z Warren, M S Shahriar, R Tripathi et al.

Interaction of laser radiation with free atoms
S Feneuille

New Journal of Physics

The open access journal at the forefront of physics

CrossMark

PAPER

High-contrast sub-Doppler absorption spikes in a hot atomic vapor cell exposed to a dual-frequency laser field

Moustafa Abdel Hafiz[1], Denis Brazhnikov[2,3,6], Grégoire Coget[1], Alexei Taichenachev[2,3], Valeriy Yudin[2,3,4], Emeric de Clercq[5] and Rodolphe Boudot[1,6]

1 FEMTO-ST, CNRS, Université de Bourgogne Franche-Comté, 26 rue de l'épitaphe, F-25000 Besançon, France
2 Institute of Laser Physics SB RAS, Novosibirsk 630090, Russia
3 Novosibirsk State University, Novosibirsk 630090, Russia
4 Novosibirsk State Technical University, Novosibirsk 630073, Russia
5 LNE-SYRTE, Observatoire de Paris, PSL Research University, CNRS, Sorbonne Universités, UPMC Univ. Paris 06, 61 avenue de l'Observatoire, F-75014 Paris, France
6 Authors to whom any correspondence should be addressed.

E-mail: brazhnikov@laser.nsc.ru and rodolphe.boudot@femto-st.fr

Abstract

The saturated absorption technique is an elegant method widely used in atomic and molecular physics for high-resolution spectroscopy, laser frequency standards and metrology purposes. We have recently discovered that a saturated absorption scheme with a dual-frequency laser can lead to a significant sign reversal of the usual Doppler-free dip, yielding a deep enhanced-absorption spike. In this paper, we report detailed experimental investigations of this phenomenon, together with a full in-depth theoretical description. It is shown that several physical effects can support or oppose the formation of the high-contrast central spike in the absorption profile. The physical conditions for which all these effects act constructively and result in very bright Doppler-free resonances are revealed. Apart from their theoretical interest, results obtained in this manuscript are of great interest for laser spectroscopy and laser frequency stabilization purposes, with applications in laser cooling, matter-wave sensors, atomic clocks or quantum optics.

1. Introduction

In recent decades, outstanding progress in laser science and technology has allowed exciting atomic physics experiments to be performed by resolving features in atomic and molecular spectra [1] with unprecedented resolution and accuracy [2]. Laser spectroscopy [3, 4] has paved the way towards tremendous and remarkable developments such as the demonstration of laser cooling and trapping techniques [5–7] or the realization of Bose–Einstein condensation in alkali gases [8], all of which have contributed to increasing our knowledge about interactions between light and matter. Laser spectroscopy of atoms and molecules is generally performed by scanning the wavelength of a laser field interacting with atoms. In conventional laser spectroscopy, closely spaced spectral lines from atomic fine or hyperfine structure are often obscured by the Doppler broadening induced by the thermal motion of atoms. Saturated absorption spectroscopy [9, 10] is an elegant technique in vapor cell experiments to overcome the Doppler broadening (Doppler-free spectroscopy) and to allow the detection of narrow natural-linewidth resonance structures in the bottom of absorption profiles. This method is frequently used as an efficient tool to stabilize the frequency of a laser to an atomic line and is applied variously in different fields including atomic frequency standards, magnetometers, laser-cooling experiments, coherent optical communications, and accurate geophysical measurements using laser interferometers. Lasers with demonstrated fractional frequency stabilities in the range 10^{-13}–10^{-11} at 1 s integration time have been demonstrated by combining saturated absorption techniques and narrow-linewidth diode lasers [11–16].

In saturated absorption spectroscopy two laser beams of the same frequency propagate in opposite directions and overlap one another through the atomic medium. When the laser frequency is far enough from

the atomic resonant frequency, the two counter-propagating waves drive different atom groups (of respective axial velocities $+v$ and $-v$) due to the Doppler shift, which yields the Doppler profile. By contrast, when the frequency detuning is being scanned near the resonance frequency, the two waves act on the same group of atoms with $v \approx 0$. Each wave reduces the absorption experienced by the other. Consequently, one can observe a Doppler-free dip in the absorption profile of one wave or a reduction in total fluorescence of the cell. This dip, with Lorentzian profile and natural linewidth, is known as the Lamb dip, or as saturated absorption resonance (SAR). It can be several orders of magnitude narrower than the Doppler-broadened spectrum in which it sits.

A simple two-level scheme (with non-degenerate energy levels) can also exhibit SAR as a single peak or with a more complex shape such as those induced by the recoil effect [17–19], high-order spatial harmonics of atomic polarization [20] or peculiarities of the Doppler effect for open atomic transitions [21]. Multilevel atoms can exhibit a complex energy-level structure involving fine and hyperfine splittings and Zeeman (magnetic) sublevels. This complex structure yields complex optical pumping processes, justifying for example the detection of cross-over resonances in saturated absorption spectra or, under appropriate conditions, a sign reversal of saturation resonances [22–27].

In a recent paper [28], an unexpected deep and narrow reversed spike (strong absorption peak) was observed in a saturated absorption experiment using a dual-frequency laser. The experiment was performed on a Cs vapor cell. The laser carrier frequency was tuned on the Cs D_1 line, with a frequency difference between the two first-order sidebands equal to the hyperfine splitting (HFS) of the ground state. This phenomenon was applied to improve by about one order of magnitude the fractional frequency stability of a diode laser compared to the usual saturated absorption technique [28], and later the frequency stability of a Cs atomic clock [29, 30, 36]. A very preliminary explanation of the phenomenon was given in [28], based on the existence of dark states and their cancellation at optical resonance. Such dark states are states non-coupled (NC) to the light, due to a quantum interference effect. They are induced by the phenomenon of coherent population trapping (CPT) [31], occurring when a common excited state is shared between two optical transitions, forming a so-called Λ scheme. Nevertheless, [28] was mainly focused on the application of this phenomenon to laser frequency stabilization without giving any complete analysis of the physics involved.

This article affords the first full explanation of this effect by reporting detailed experimental investigations and an in-depth theoretical analysis. Actually, several physical phenomena are involved in the SAR reversal. These phenomena are coherent superposition states of Zeeman sublevels (CPT effect) inside a hyperfine (HF) state and between HF states, the Hanle effect, and velocity-selective optical pumping effects. Their experimental demonstration is reported in section 2, which summarizes a wide variety of experimental results obtained using an experimental setup based on a single laser source. Tests are performed in the single-frequency and dual-frequency regimes. The detection of dark states under appropriate conditions in the bottom of the enhanced-absorption reversed spike is clearly reported, using Hanle resonances or optical CPT resonances. Section 3 describes the theoretical formalism, based on the density matrix approach, of the main processes involved in the reported experiments. We show that the various experimental observations can be fully described by considering separate simple three-level atomic Λ-schemes. A discussion is reported at the end of the manuscript to provide a clear and rigorous link between experimental tests and the theoretical section, highlighting for the main experimental figures which of the numerous processes involved contributes dominantly to the experimental observation.

Apart from its undeniable theoretical interest, the phenomenon addressed can be of great interest for laser frequency standards and for stabilization of the carrier frequency of a modulated laser when the carrier frequency is out of resonance with an atomic transition, with application to laser cooling, matter-wave interferometers, atomic clocks and magnetometry.

2. Experimental tests and results

This section aims to report a significant number of experimental tests in order to highlight properties of the Doppler-free spectroscopy in single- or dual-frequency regimes. Tests are performed with a single modulated laser source described in the following.

2.1. Experimental setup

Figure 1 shows the experimental setup used to perform Doppler-free spectroscopy in Cs vapor cells. The laser source is a 1 MHz distributed feedback (DFB) diode laser tuned on the Cs D_1 line at 894.6 nm. An optical isolation stage (~70 dB) is used to prevent optical feedback. A pigtailed mach–Zehnder electro-optic modulator (EOM—Photline NIR-MX800-LN), driven at 4.596315 GHz by a low-noise microwave frequency synthesizer [32], allows the generation of two first-order optical sidebands whose frequency splitting is tuned around $\nu_g = 9.192631\,\text{GHz}$, the HFS of the Cs ground state. The optical carrier is actively suppressed by the technique

Figure 1. Experimental setup. DFB: distributed feedback diode laser, ISL: isolator, HWP: half-wave plate, EOM: Mach–Zehnder electro-optic modulator, LO: microwave frequency synthesizer, PBS: polarizing beam splitter cube, BS: beam splitter cube, QWP: quarter-wave plate, M: mirror, PD: photodiode, DAQ: data acquisition card. The inset on the right shows the energy structure of the Cs D_1 line.

Figure 2. Absorption profiles in the single-frequency laser regime. The laser power incident in the cell is 200 μW. (a) Parallel linear polarizations; (b) crossed linearly polarized beams are used. For (a) and (b), the static magnetic field is 0 or 490 mG. For (b), an offset of 0.005 V is added to the data for $B = 0$ in order to distinguish the orientation of the dip correctly. The origin of the frequency axis is chosen arbitrarily.

presented in [33]. The contribution of second-order and third-order optical sidebands is rejected at a level 25 to 35 dB lower, and is neglected. The output light beam is thus close to a pure bichromatic laser beam. At the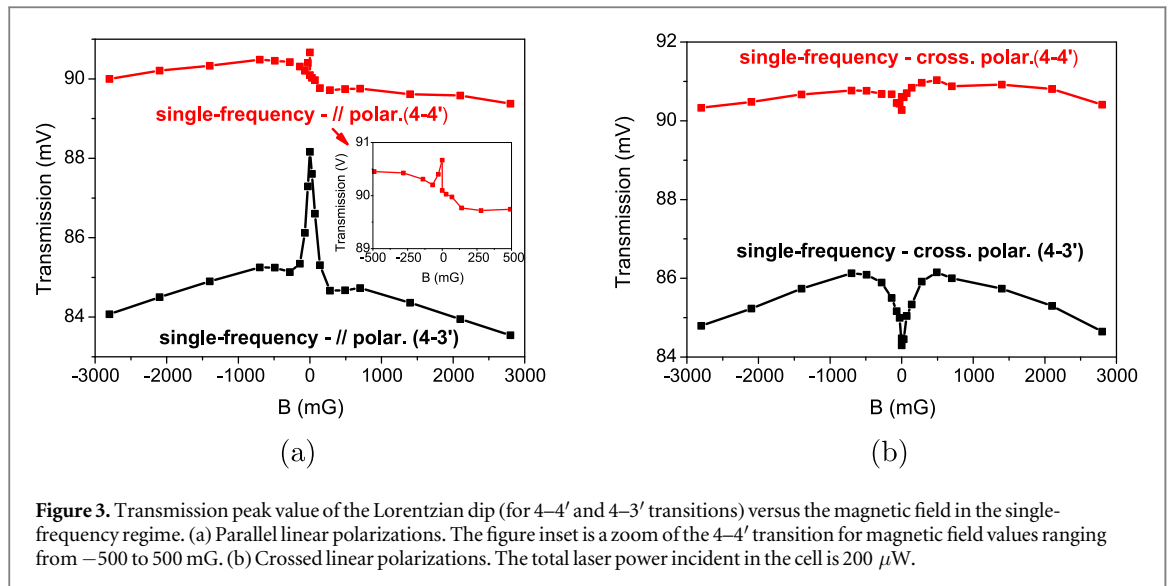 output of the EOM, a fiber collimator is used to extract a free-space collimated laser beam with a diameter of about 2 mm. A fraction of the laser power is extracted to perform the Doppler-free spectroscopy setup. The laser beam is sent and reflected back in an evacuated Cs vapor cell that is 2 cm in diameter and 2 cm long. A quarter-wave plate, placed between the cell and the reflection mirror, can be adjusted such that propagating and counter-propagating beams are polarized linearly and parallel, or else mutually orthogonally. The power of the reflected beam is measured by a photodiode. The cell is not temperature-stabilized. All tests were performed at ambient temperature (about 22.5 °C). The cell is surrounded by a mu-metal magnetic shield to prevent magnetic perturbations from the environment. A static magnetic field, parallel to the axis of light propagation, can be applied with a solenoid surrounding the cell.

2.2. Single-frequency regime: Zeeman CPT

In this section, the microwave power driving the EOM is turned off. The usual Doppler-free spectroscopy with a single laser frequency is performed. Here and in the following, the optical transitions will be denoted only by the HF numbers F–F' of the levels involved. Figures 2(a) and (b) show the 4–4′ and 4–3′ transitions for counter-propagating parallel or crossed polarizations respectively, with two different static magnetic field values of 0 and 490 mG. The presence of a static magnetic field tends to increase the depth of the Doppler-broadened absorption profile for the 4–3′ transition. This is also observed on the 4–4′ transition but with a reduced strength. For parallel polarizations, the usual Doppler-free dip is observed. For orthogonally polarized counter-propagating beams, at null magnetic field, we clearly observe that the 4–3′ dip is cancelled or even slightly reversed. Note that at 'high' magnetic field, there is no significant difference between absorption profiles of the two polarization schemes.
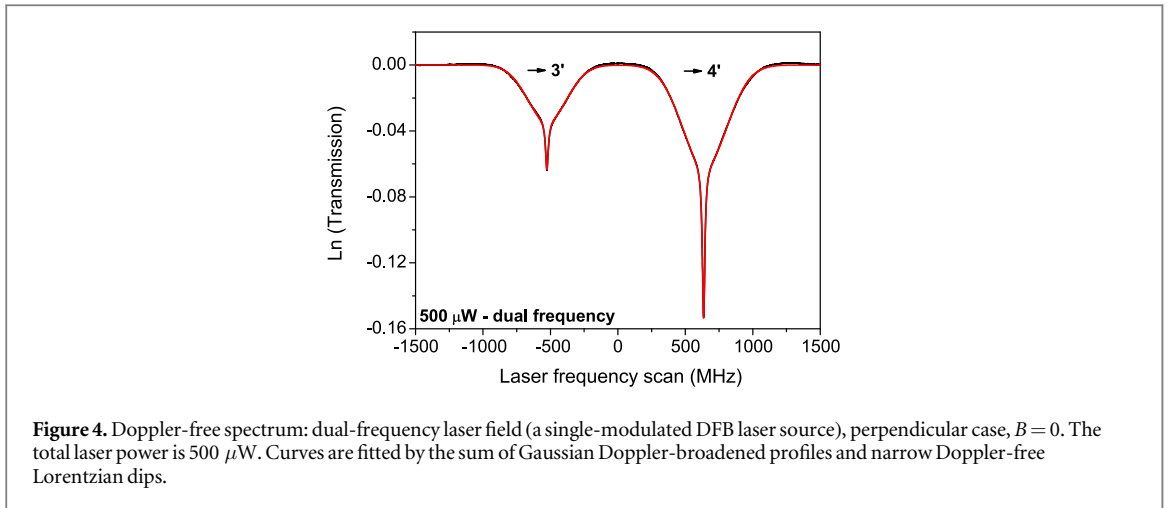
This behavior will be explained theoretically in section 3.2. Briefly, at low magnetic field, a linearly polarized wave, traveling along the quantization axis $\hat{z}$, pumps atoms in a state superposition of m_F Zeeman sublevels, such that Δm_F, the difference of m_F, is even. These states, so-called 'dark' (or NC) states [34], are uncoupled

Figure 3. Transmission peak value of the Lorentzian dip (for 4–4′ and 4–3′ transitions) versus the magnetic field in the single-frequency regime. (a) Parallel linear polarizations. The figure inset is a zoom of the 4–4′ transition for magnetic field values ranging from −500 to 500 mG. (b) Crossed linear polarizations. The total laser power incident in the cell is 200 μW.

from light, explaining the low absorption. This is the CPT phenomenon. When the magnetic field strength increases, the Zeeman sublevels of the ground state are frequency-split and no longer satisfy the two-photon resonance, and the transparency of the vapor cell decreases. This explains why the Doppler absorption profiles of the 4–3′ as well as 4–4′ transitions are deeper when the magnetic field is on (compare black and red curves in figure 2). This effect is lower on the 4–4′ transition for two main reasons. Firstly, the probability for the 4–4′ transition is weaker than for the 4–3′ transition (the ratio between the two spectral line strengths is 7/5 in favor of the 4–3′ transition). Secondly, the branching ratio for the 4–4′ transition is smaller than for the 4–3'. The latter leads to a considerable optical pumping of atoms to the non-resonant ground level $F = 3$ when the 4–4′ transition is being excited.

It should also be noted that the central resonance structure is very sensitive to the polarizations of the light waves but also to the branching ratio of certain atomic transitions (these features will be considered further in the theoretical section). In particular, one can observe an increase in the transparency at the center of the resonance for parallel light polarizations for the 4–3′ transition (figure 2(a), left black resonance) and a slight increase in absorption in the case of crossed polarizations (figure 2(b), left black resonance). In the same conditions, the central resonance for the weak 4–4′ transition (right black resonances in figures 2(a) and (b)) is almost insensitive to the light polarizations and always appears as a peak in transparency. At optical resonance and at low magnetic field, only the atoms of axial velocity close to zero can absorb the light field. These atoms are resonant with both travelling and counter-propagating waves. As explained in section 3.2, in the parallel polarization scheme, dark states are common to both fields and no change occurs: the regular dip in saturated absorption is observed. In contrast, in the case of crossed polarizations, the respective dark states are mutually orthogonal and cancel each other (see section 3.2). In this case, the absorption increases, counterbalancing the regular dip.

The last interpretation is sustained by transmission curves as a function of the magnetic field. We have recorded absorption spectra (4–4′ and 4–3′ transitions) versus the static magnetic field. Parallel or orthogonally linearly polarized counter-propagating beams were tested. The direction of solenoid current was changed to apply 'negative-sign' magnetic fields. Figure 3(a) shows the transmission peak value signal, for parallel-polarization counter-propagating beams, for different values of the static magnetic field B. The maximum transmission level is increased around the null magnetic field value. As explained above, this resonance peak is due to the existence of atoms in dark states that vanish at higher magnetic field strength. The reported spectra represent the regular magneto-optical Hanle resonances observed with counter-propagating light waves [35]. The weakness of the 4–4′ transition explains why the amplitude and linewidth of the central peak are smaller for this transition. With crossed linear polarizations (see figure 3(b)) the decrease in transmission observed at null magnetic field for both transitions is explained by the absence of a dark state common to both counter-propagating waves. With increasing B values, most of the CPT resonances become out of resonance. The usual saturated absorption scheme is observed again and the absorption peak becomes a regular saturated dip (see figure 2). Here again, the effect is reduced for the 4–4′ transition. The background resonance (pedestal of the central narrow peak) is due to the velocity-selective saturation effect, which regularly takes place in a gas of atoms interacting with resonant light waves. This resonance structure can be attributed to the regular saturated-

Figure 4. Doppler-free spectrum: dual-frequency laser field (a single-modulated DFB laser source), perpendicular case, $B = 0$. The total laser power is 500 μW. Curves are fitted by the sum of Gaussian Doppler-broadened profiles and narrow Doppler-free Lorentzian dips.

absorption resonance whose width is of the order of 10 G. The asymmetry in the curve is attributed to a change in the laser power between records of spectra related to the right and left parts of the figures.

Using repumping radiation, one can expect that both 4–3′ and 4–4′ transitions will exhibit a noticeable narrow dip at the center of transmission curves. Nevertheless, this additional coherent radiation in the dual-frequency regime does not act only as a repumping field. Indeed, if we have two mutually coherent waves driving adjacent optical transitions (for instance, 3–4′ and 4–4′), other types of dark states can be created, involving magnetic sublevels of different hyperfine levels of the ground state $6^2S_{1/2}$. These dark states can also lead to observation of a high-contrast absorption peak at the center of the profile, as well as CPT states involving magnetic sublevels of one single hyperfine level. Corresponding details will be considered in the theory section.
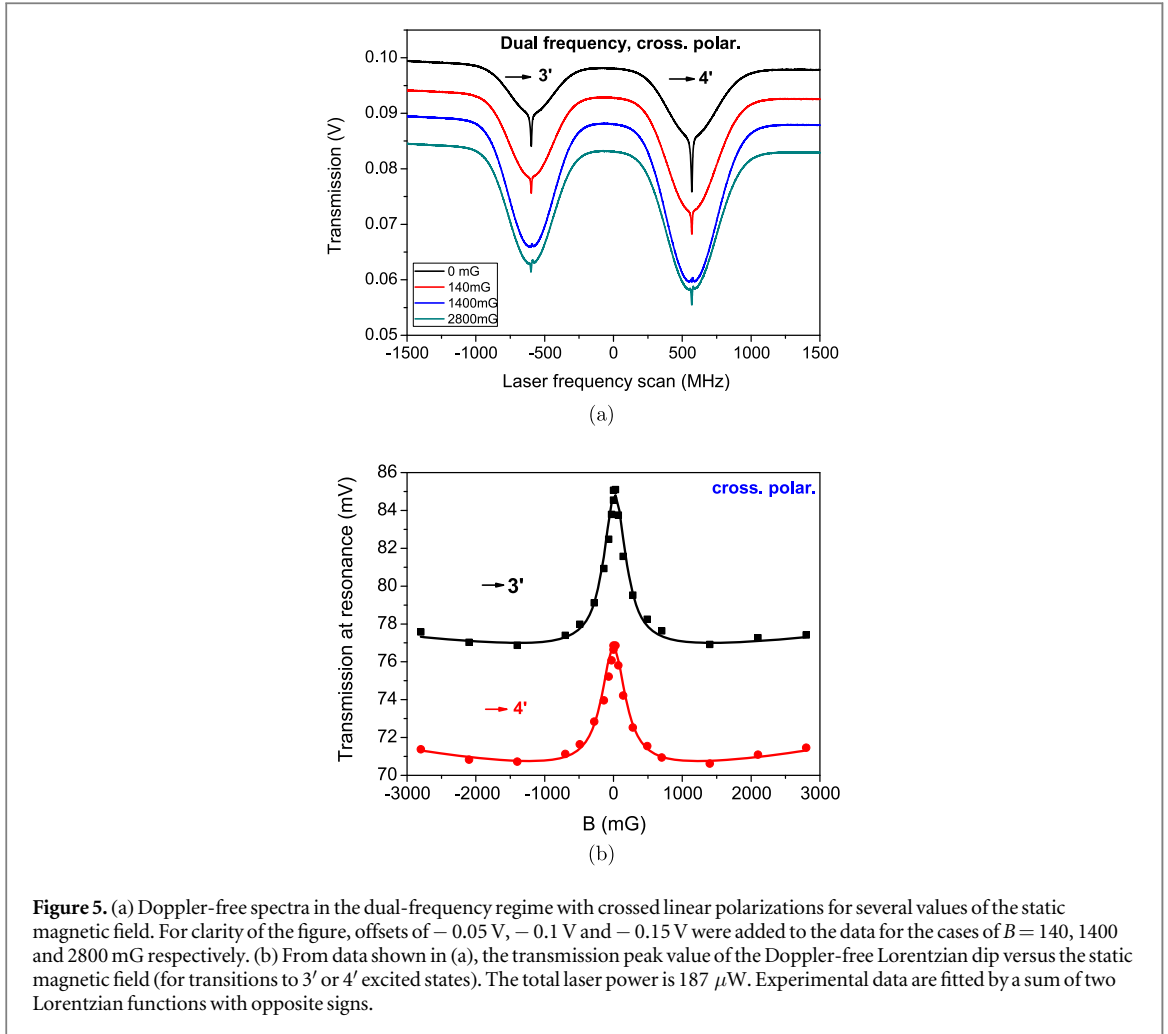
2.3. Dual-frequency regime: Zeeman and HFS CPT

2.3.1. Basic approach

In this section, the EOM is driven at $\nu_g/2$. A dual-frequency SAR spectroscopy is performed. In a first approach, figure 4 shows typical Doppler-free spectra observed in the Cs cell at null magnetic field when a dual-frequency laser field and crossed linear polarizations are used. For the dual-frequency case, transitions are labelled only by F', the HF number of the common excited state. A significant sign reversal of the dip and a large increase in Doppler-free atomic absorption are observed, especially at high laser power. This behavior was recently reported in [28]. As in the previous section, Zeeman coherences are built but now in each HF level. Moreover, microwave hyperfine coherences are also built as reported in section 3.1. At resonance (null detuning of both optical transitions), atoms of null axial velocity are resonant with both counter-propagating beams. In the case of crossed polarization, Zeeman CPT states built by a beam are destroyed by the reversed beam, like the HFS-CPT states, leading to a Doppler-free enhancement of the absorption. This observation is in good agreement with theoretical explanations reported in section 3. In [28], we studied the FWHM, signal (amplitude) and amplitude/FWHM ratio of the Doppler-free Lorentzian dip versus the laser power. We observed that the power broadening of the single-frequency dip is larger than in the dual-frequency case. Simultaneously, the amplitude of the dip is dramatically increased in the dual-frequency case, especially when the $F' = 4$ excited state is connected. In the single-frequency case, the atomic system is an open system, causing the atoms to be pumped into the other hyperfine ground state and leading to a higher effective saturation parameter. Conversely, in the dual-frequency regime, the atomic system is closed, avoiding the loss of atoms.

2.3.2. Impact of the static magnetic field

Figure 5(a) shows the transitions to 3′ and 4′ excited states, in the dual-frequency regime, with orthogonally polarized counter-propagating beams, for different values of the static magnetic field. We first observe an absorption spike at null magnetic field. On increasing the magnetic field, the spike is progressively reduced and becomes a peak of transmitted light. For higher magnetic fields, the peak reverses again in an absorption spike. The depth of the Doppler-broadened profile is increased with the magnetic field because of the suppression of CPT states as in figure 2(b). Nevertheless, in terms of transmission at exact resonance, we observe a reduction in the transmission with increased magnetic field up to about 1 G and then again a very slight increase, see figure 5(b). For both transitions, experimental data are fitted by a sum of two Lorentzian functions with opposite signs. The central transmission peak is the Hanle resonance due to the creation of the Zeeman and HF coherences (see section 3). This resonance can be significantly narrower than the homogeneous linewidth. The wide background dip is the manifestation of saturation and optical pumping effects. For the 4′ transition, the
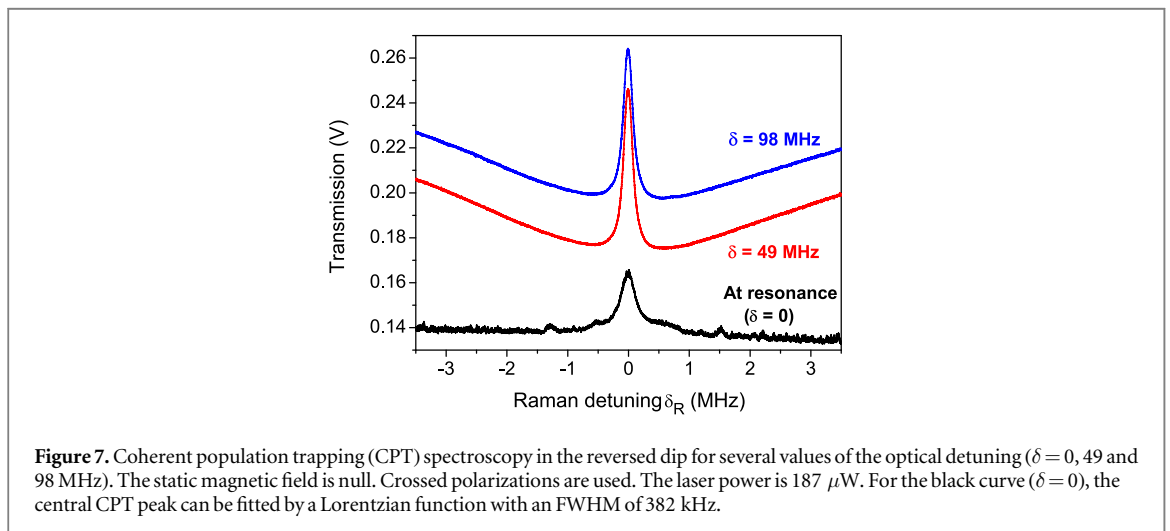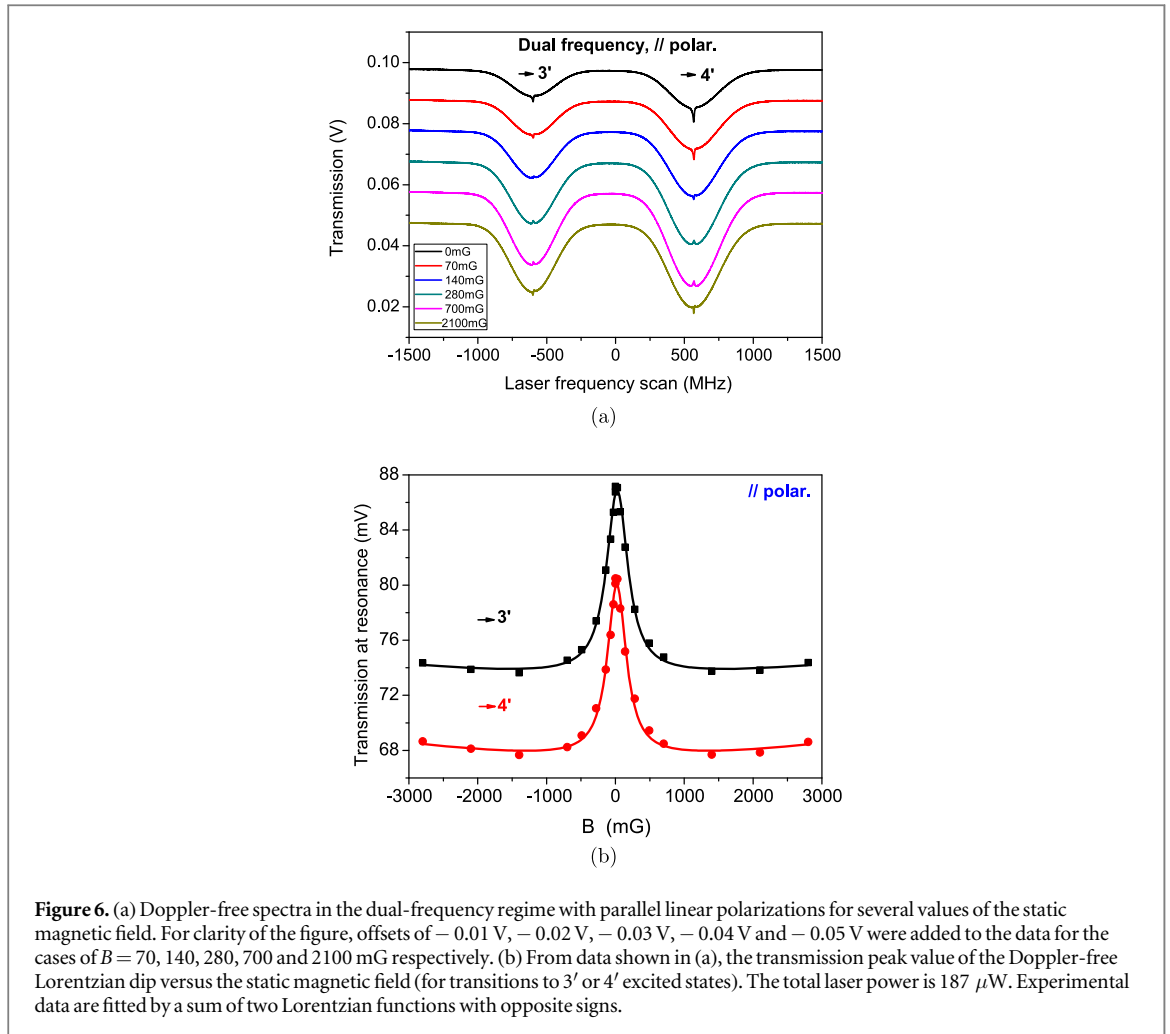
Figure 5. (a) Doppler-free spectra in the dual-frequency regime with crossed linear polarizations for several values of the static magnetic field. For clarity of the figure, offsets of -0.05 V, -0.1 V and -0.15 V were added to the data for the cases of $B = 140$, 1400 and 2800 mG respectively. (b) From data shown in (a), the transmission peak value of the Doppler-free Lorentzian dip versus the static magnetic field (for transitions to 3' or 4' excited states). The total laser power is 187 μW. Experimental data are fitted by a sum of two Lorentzian functions with opposite signs.

FWHM of the central Lorentzian function is about 420 mG, yielding a Raman detuning for ($\Delta m_F = 2$) Zeeman coherences of about 294 kHz. The Raman detuning δ_R is equal to the frequency difference between the two components of the laser beam, Δ_L, minus the splitting ν_g of the two ground-state sublevels, $\delta_R = \Delta_L - \nu_g$. As reported in the next subsection (see the black curve of figure 7), the detected CPT resonance exhibits an FWHM of about 382 kHz, a value comparable to the value extracted from figure 5(b), taking into account the large uncertainty on the fit parameters due to the small number of points delimiting the broad Lorentzian curve.

We performed a similar study in the dual-frequency regime using counter-propagating linear parallel polarizations. Figures 6(a) and (b) summarize these results. At null magnetic field and if only Zeeman CPT was involved, we expected the dip to be regular (increased transmission). This behaviour is observed experimentally at low laser power. At higher laser power, as in figure 6(a), the Doppler-free dip is observed to be reversed (increased absorption), then regular for magnetic field values up to about 1 G and reversed again after. The change in orientation of the dip with some experimental conditions (such as the laser power or the magnetic field) is not so surprising. Indeed, it is important to note again that the Doppler-free dip observed in the center of the absorption profile results from the competition of Zeeman-CPT states, HFS-CPT states and optical pumping effects, as discussed in section 3.4. Thus, the main orientation of the dip will result in real experimental conditions depending on the respective strengths and the sum of these contributions.

2.3.3. Coherent population trapping spectroscopy in the reversed dip

We have performed microwave hyperfine CPT spectroscopy in the bottom of the reversed dip in order to demonstrate the HFS-CPT resonances. Tests were performed using the transition to the 4' excited state. For this purpose, the laser frequency is either tuned on the extremum of the reversed dip (null optical detuning, $\delta = 0$) or is slightly shifted from optical resonance ($\delta \neq 0$). More precisely, the laser carrier frequency ν_L (before the EOM) is tuned between the middle of the ground-state HFS and the $F' = 4$ level. The optical detuning is then defined as $\delta = \nu_L - (\nu_{4'3} + \nu_{4'4})/2$, with ν_{ji} the frequency of the optical transition ($F = i - F' = j$). For these different points of operation of laser frequency detuning, the laser is not frequency-stabilized and the microwave signal frequency that drives the EOM is swept around $\nu_g/2$ (i.e. δ_r is swept around 0). These tests were performed

Figure 6. (a) Doppler-free spectra in the dual-frequency regime with parallel linear polarizations for several values of the static magnetic field. For clarity of the figure, offsets of -0.01 V, -0.02 V, -0.03 V, -0.04 V and -0.05 V were added to the data for the cases of $B = 70$, 140, 280, 700 and 2100 mG respectively. (b) From data shown in (a), the transmission peak value of the Doppler-free Lorentzian dip versus the static magnetic field (for transitions to $3'$ or $4'$ excited states). The total laser power is 187 μW. Experimental data are fitted by a sum of two Lorentzian functions with opposite signs.

Figure 7. Coherent population trapping (CPT) spectroscopy in the reversed dip for several values of the optical detuning ($\delta = 0$, 49 and 98 MHz). The static magnetic field is null. Crossed polarizations are used. The laser power is 187 μW. For the black curve ($\delta = 0$), the central CPT peak can be fitted by a Lorentzian function with an FWHM of 382 kHz.

in different configurations including null or fixed values of the static magnetic field in crossed polarizations. A typical spectrum detected in the bottom of the reversed dip at null magnetic field is shown in figure 7 for crossed polarizations.

We observe that the amplitude of the CPT resonance is considerably reduced under the condition of exact optical resonance ($\delta = 0$). When the one-photon detuning is sufficiently far from zero ($\delta \gg \gamma$, with γ half the natural linewidth of the optical transition, about 2.3 MHz for the Cs D_1 line), we detect in figure 7 transparency peaks with a large amplitude. The behavior of the resonance curve is quite clear. For $\delta \gg \gamma$, the counter-propagating laser beams are resonant for atoms of two separate velocity groups having axial velocities

Figure 8. CPT spectroscopy in the reversed dip for two values of the optical detuning ($\delta = 0$ and 49 MHz) with application of a static magnetic field ($B \sim 1.4$ G). Crossed polarizations are used.
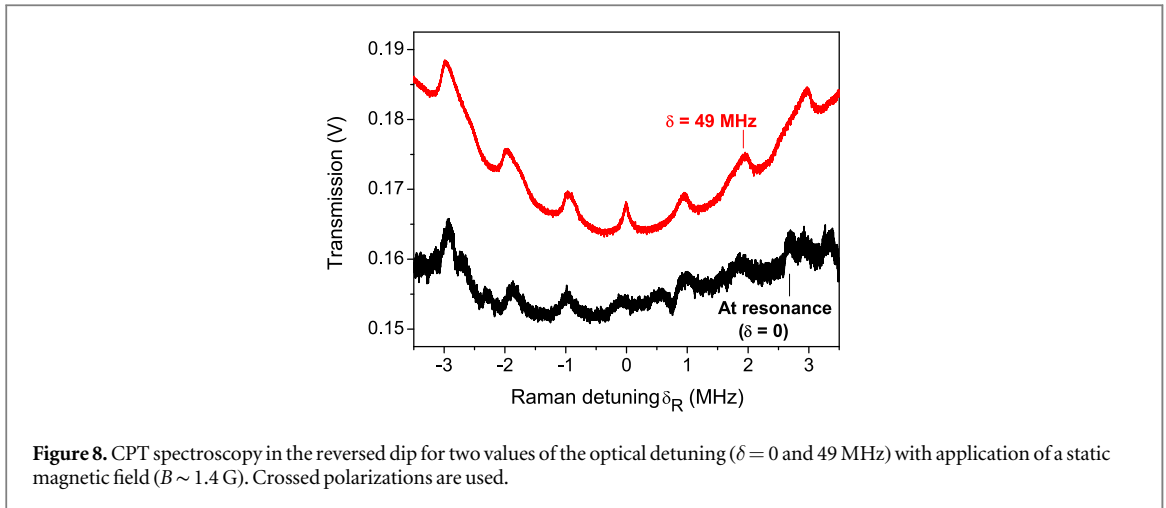
$\nu = -2\pi\delta/k$ and $\nu = +2\pi\delta/k$ ($\approx$40 m s^{-1} for $\delta = 49$ MHz), with k the wavevector. Atoms in each of these two groups are optically pumped into Zeeman and HFS dark states. The narrow central resonance in figure 7 is the HFS-CPT resonance. At optical resonance ($\delta = 0$), with almost equal amplitudes ($E_1 \approx E_2$) and crossed linear polarizations, Zeeman-CPT states do not occur as seen above. Therefore, absorption of the light field is enhanced at exact optical resonance (compare black and red curves in figure 7 at $\delta_R = 0$).

As will be shown in the theory section, HFS dark states can be produced by the two counter-propagating beams in some regions of the cell and can be suppressed in others, whatever the polarizations. This explains the observation of a narrow HFS-CPT resonance in the center of the black curve of figure 7. We note that the amplitude of CPT resonances in the case of parallel polarized counter-propagating beams was measured to be comparable for the regimes $\delta = 0$ and $\delta \gg \gamma$. This is the manifestation of the HFS-CPT and Zeeman-CPT effects, which occur for the resonant velocity groups $\nu = \pm 2\pi\delta/k$, for $\delta \gg \gamma$ as well as for $\delta = 0$.

An additional experiment similar to the one just described was performed by applying a static magnetic field. Corresponding spectra are reported in figure 8, where crossed polarizations are used. Again, at null optical detuning, the CPT resonance is almost not present. At non-null optical detuning, the Zeeman spectrum is clearly visible. The seven peaks observed correspond to two-photon transitions ($\Delta F = 1$, $\Delta m_F = 0$, ± 2) involving Zeeman sublevels of different hyperfine ground-state levels $F = 3$ and $F = 4$. The central transition is narrower than neighboring transitions, due to the fact that the magnetic sensitivity of Λ-schemes involved in the central transition is lower than that of Λ-schemes involved in adjacent transitions. Moreover, a residual inhomogeneity of the magnetic field in the cell could affect the widths of these resonances differently.

These experiences demonstrate clearly that at null magnetic field: (i) HFS-CPT states are present at null Raman detuning, (ii) the CPT amplitude is reduced but non-null at optical resonance $\delta = 0$ in crossed polarizations, (iii) the CPT amplitude is higher for non-null optical detuning, (iv) HFS-CPT effects can contribute to the observation of the Doppler-free reversed dip in the dual-frequency regime.

2.3.4. Impact of the HFS-CPT states

The goal of this experiment was to discriminate the effects of Zeeman coherences and HF coherences on the dip reversal. HF coherences are not created when both optical sidebands excite two optical transitions without any common excited state, or are nearly cancelled for large Raman detuning, while Zeeman coherences are still present. Here, the Mach–Zehnder EOM is driven by a commercial synthesizer (Rohde-Schwarz SMB100A). The cell is protected by magnetic shielding and no static magnetic field is applied. Data acquisition is performed as a function of the laser frequency scan, for orthogonally polarized or parallel polarized counter-propagating beams.

Figures 9(a)–(d) summarize measurements performed in different configurations. Each of these figures is obtained for a given Raman detuning value and presents two spectra obtained in the respective cases of crossed or parallel polarizations. Figures 9(a) and (b) report measurements performed with large Raman detunings (the EOM is driven at $\nu_g/2 \pm \nu_e/2$, with $\nu_e = 1.167$ GHz, the HF splitting of the excited state). For Doppler-free resonances on the left and right sides of figures 9(a) and (b), only one laser frequency is resonant with an atomic transition (see the insets). In such a case the regular SAR profiles are observed, whose amplitudes are reduced by optical pumping in the non-resonant HF ground-state levels and by the Zeeman-CPT effect. In the case of the central profile, both frequency components of the optical fields are at resonance, but with two separate HF excited levels. In this configuration, Zeeman coherences can still be created between magnetic sublevels of the same HF level, but HF coherences cannot. We observe a deeper Doppler profile (no atom leakage by optical
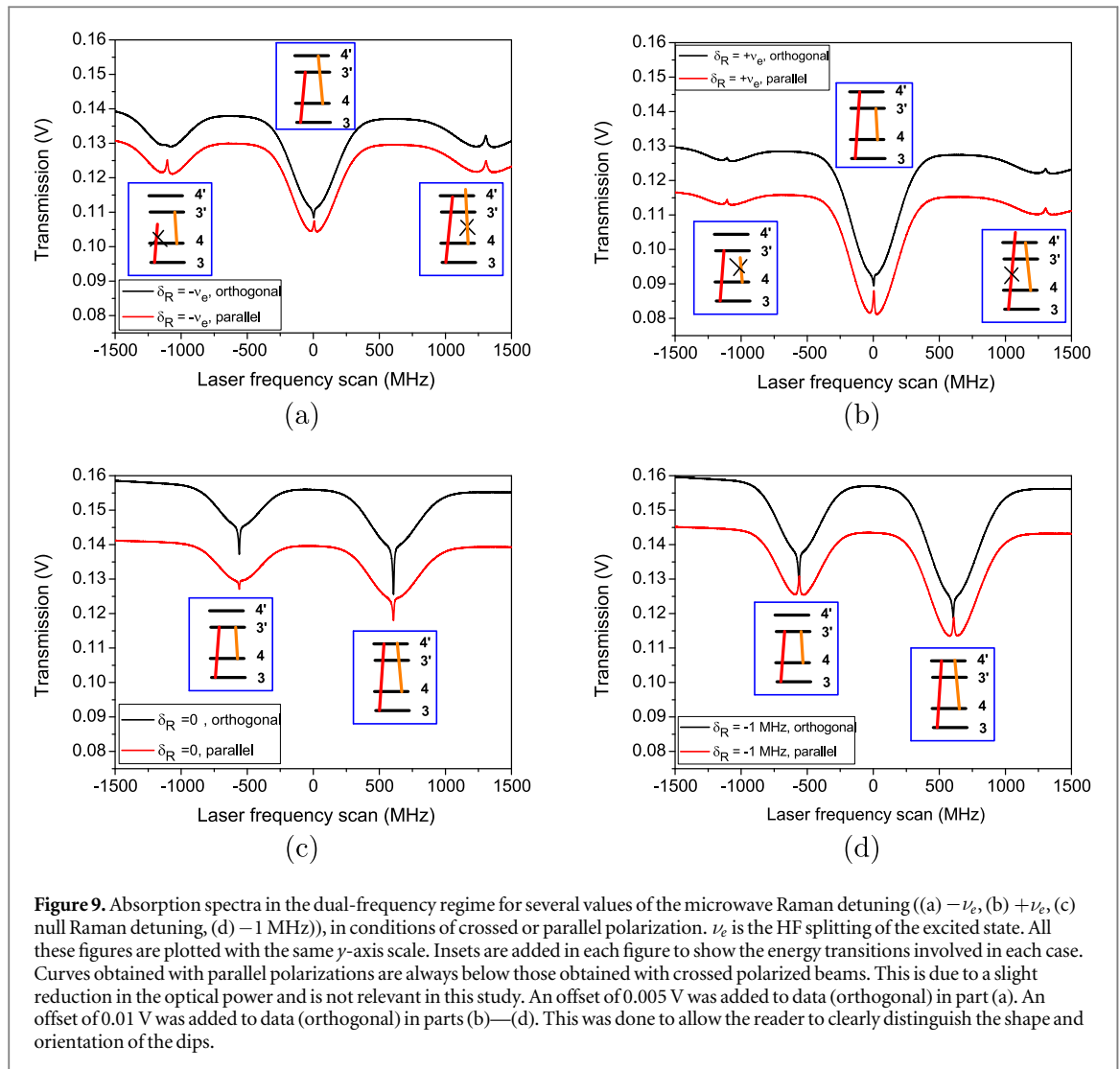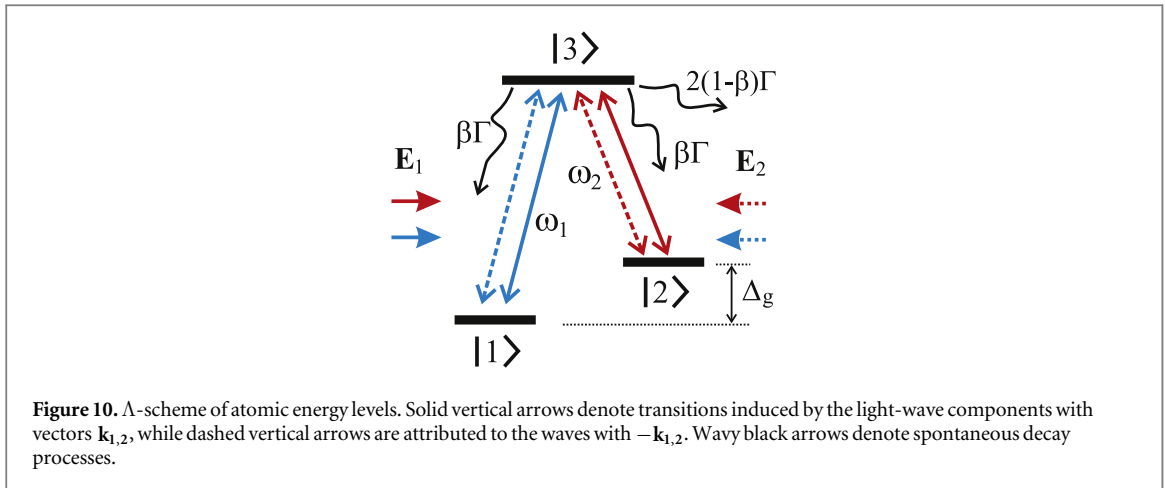
Figure 9. Absorption spectra in the dual-frequency regime for several values of the microwave Raman detuning ((a) $-\nu_e$, (b) $+\nu_e$, (c) null Raman detuning, (d) -1 MHz)), in conditions of crossed or parallel polarization. ν_e is the HF splitting of the excited state. All these figures are plotted with the same *y*-axis scale. Insets are added in each figure to show the energy transitions involved in each case. Curves obtained with parallel polarizations are always below those obtained with crossed polarized beams. This is due to a slight reduction in the optical power and is not relevant in this study. An offset of 0.005 V was added to data (orthogonal) in part (a). An offset of 0.01 V was added to data (orthogonal) in parts (b)—(d). This was done to allow the reader to clearly distinguish the shape and orientation of the dips.

pumping), at the bottom of which a Doppler-free dip is detected. A regular (enhanced transmission) SAR dip is observed in the case of parallel polarizations; the Zeeman dark states are common to both counter-propagating waves. In contrast, the central Doppler-free dip is reversed with orthogonal polarizations, because Zeeman dark states ($\Delta F = 0$, $\Delta m_F = 2$) created in each HF level by a travelling wave are destroyed by the counter-propagating wave at null optical detuning.

In figures 9(c) and (d), a common excited state is shared between optical transitions: at null Raman detuning, $\delta_R = 0$, in figure 9(c), or with $\delta_R = 1$ MHz in figure 9(d). Figure 9(c) describes the case addressed in the previous subsections. Here, HF and Zeeman coherences are created together. We observe a modest Doppler profile, while the Doppler-free dip is enhanced. The amplitude of the Doppler profile is reduced by CPT states created in the velocity groups for which the fields are at resonance. At optical resonance, in crossed polarizations, HF and Zeeman dark states are cancelled and the absorption is significantly enhanced, leading to the clear high-contrast central reversed dip. In figure 9(d), the HF coherences are nearly cancelled, because the Raman detuning is too high, leading to a deeper Doppler profile. With crossed polarizations the dip is still reversed but reduced, and induced only by the cancellation of Zeeman coherences.

The effect of HF coherences is highlighted by comparing figures 9(c) and (d) in the case of parallel polarization. Without HF coherences (figure 9(d)) the dip is a regular SAR dip, as expected, since there is no increase in absorption by the wipeout of Zeeman dark states at optical resonance. In contrast, the dip is reversed when HF dark states are present (figure 9(c)). This shows that the HF dark states, or at least an important part of them, are destroyed at optical resonance, even for linear polarizations. At high laser power, this effect is larger than the regular dip that would be induced by Zeeman coherences. This will be explained in section 3.1 by the phase shift of both running waves.

In summary, both Zeeman and HFS CPT lead to a reduced Doppler profile for both polarization cases. Zeeman CPT alone (see figures 9(a), (b), (d)) leads to a regular SAR dip in parallel polarizations, and an inverted peak in crossed polarizations. HFS CPT reverses the regular dip in parallel polarizations and increases the size of

Figure 10. Λ-scheme of atomic energy levels. Solid vertical arrows denote transitions induced by the light-wave components with vectors $\mathbf{k}_{1,2}$, while dashed vertical arrows are attributed to the waves with $-\mathbf{k}_{1,2}$. Wavy black arrows denote spontaneous decay processes.

the absorption peak in crossed polarizations (see figure 9(c)). These observations are in agreement with predictions of our simplified theoretical model, as discussed in section 3.4.

3. Theoretical analysis

A full theoretical description of the high-contrast absorption spike observed in the dual-frequency regime (see figure 4), taking into account the real complex structure of atomic energy levels, light wave polarizations, and various optical pumping and nonlinear coherent processes, is quite a difficult task. Here, we propose a simplified spectroscopic model based on a three-level Λ-scheme that allows to understand the main physical reasons underlying the formation of the high-contrast resonance spike. The scheme is shown in figure 10. Despite its apparent simplicity, this scheme can explain the impact of the static magnetic field, the two-photon (Raman) detuning, light wave polarizations or mutual coherence between the frequency components of the light field observed in the experiments. We focus here on analyzing the specific case where the highest spike amplitude is obtained. As seen in figure 4, this occurs when all light waves interact with the excited atomic state $F' = 4$. In general, at least three physical effects can contribute to formation of the central spike. In this section, we consider them separately to understand qualitatively the main features of each effect.

Let us first describe the density matrix formalism applied to our system. We assume that the Λ-scheme interacts with a dual-frequency laser field composed of two counter-propagating, linearly polarized plane waves. The Cartesian coordinate system is oriented such that the polarization of the first dual-frequency wave (E_1) is directed along the x axis, while the related wavevectors $\mathbf{k}_1$ and $\mathbf{k}_2$ are parallel to the quantization axis z. Under this orientation of the system, linearly polarized light can be represented by two polarization components, σ^+ and σ^-, in the cyclic basis. If a real atomic transition is considered (taking into account degeneracy of energy levels), these two σ components induce corresponding $\sigma^{\pm}$ optical transitions in the atom. Thus, if the linear polarization has an angle ϕ between the direction of polarization and the x axis, the σ^- and σ^+ polarization components acquire additional phase shifts $\exp(\pm i\phi)$. Since we use a simplified spectroscopic model, instead of considering many magnetic sublevels, the orientation of polarization can be included in our model with the help of phase shifts $\exp(\pm i\phi)$ if we assume that $|1\rangle \rightarrow |3\rangle$ and $|2\rangle \rightarrow |3\rangle$ transitions of the Λ-scheme (see figure 10) are induced by σ^+ and σ^- polarization components respectively. Following this, we come to the expression for the light field:

$$
\begin{aligned}
E(z,\, t) = {} & E_1[\mathrm{e}^{-\mathrm{i}(\omega_1 t - k_1 z)} + \mathrm{e}^{-\mathrm{i}(\omega_2 t - k_2 z)}] \\
& + E_2[\mathrm{e}^{-\mathrm{i}(\omega_1 t + k_1 z - \phi + \phi_1)} + \mathrm{e}^{-\mathrm{i}(\omega_2 t + k_2 z + \phi + \phi_2)}] + \text{c.c.}
\end{aligned}
\tag{1}
$$

We would like to emphasize that the light wave E_1 is travelling in the same direction as the z axis and has two frequency components (ω_1 and ω_2), while E_2 is a counter-propagating wave with the same frequency components. As seen from equation (1), we assume that both frequency components of each wave have equal real amplitudes (just for simplicity). The angle ϕ is the mutual angle between linear polarizations of counter-propagating waves. We will concentrate further on two principal cases: $\phi = 0$ and $\phi = \pi/2$. Since the field E_2 is formed by the reflection of the field E_1, it has a certain spatial phase shift (actually, two different shifts $\phi_{1,2}$ for each frequency component as the lengths of the wavevectors $\mathbf{k}_1$ and $\mathbf{k}_2$ are different). The acronym 'c.c.' stands for the complex conjugate.

In the case of a dilute gas, collisions between atoms can be neglected. Moreover, we do not take into account exchange of linear momentum between an atom and a photon, leading to the recoil effect. Thus, the problem

can be considered with the help of a one-atom density matrix in the Wigner representation $\hat{\rho}(z, v, t)$ according to equation [9]

$$\frac{\mathrm{d}\hat{\rho}}{\mathrm{d}t} = -\frac{\mathrm{i}}{\hbar}[(\widehat{H}_0 + \widehat{V}), \hat{\rho}] + \widehat{\mathcal{R}}\{\hat{\rho}\}. \tag{2}$$

Here $\mathrm{d}/\mathrm{d}t = \partial/\partial t + v \, \partial/\partial z$ with v the projection of the atom's velocity on the z axis. The Hamiltonian $\widehat{H}_0$ of a free atom in the basis of eigenfunctions can be written as

$$\widehat{H}_0 = \sum_{n=1}^{3} \mathcal{E}_n |n\rangle \langle n|, \tag{3}$$

where $\mathcal{E}_n$ are energies of the corresponding levels (see figure 10). Further transition frequencies of the arms of the Λ-scheme will be denoted $\omega_{mn} = (\mathcal{E}_m - \mathcal{E}_n)/\hbar$, with $\hbar = h/(2\pi)$, h being the Planck constant. Taking into account equation (1), non-zero matrix elements of the interaction operator $\widehat{V}$ in the rotating-wave approximation (RWA) and the approximation of electric-dipole interaction have the following forms:

$$V_{31} = \langle 3|\widehat{V}|1\rangle = -\hbar e^{-\mathrm{i}\omega_1 t}[\Omega_{R1}e^{\mathrm{i}k_1 z} + \Omega_{R2}e^{-\mathrm{i}(k_1 z + \phi_1)}],$$
$$V_{32} = -\hbar e^{-\mathrm{i}\omega_2 t}[\Omega_{R1}e^{\mathrm{i}k_1 z} + \Omega_{R2}^* e^{-\mathrm{i}(k_2 z + \phi_2)}], \tag{4}$$

where $\Omega_{R1} = dE_1/\hbar$ and $\Omega_{R2} = (dE_2/\hbar)e^{-\mathrm{i}\phi}$ are the Rabi frequencies, and we assume two arms of the Λ-scheme to have equal and real dipole moments d. Other non-zero matrix elements V_{13} and V_{23} can be obtained from the expressions (4) by conjugate transpose operations, because the interaction operator is Hermitian, $\widehat{V} = \widehat{V}^\dagger$.

All the relaxation processes are considered in the frame of the widely used approach of relaxation constants. The explicit form for the relaxation operator $\widehat{\mathcal{R}}$ is

$$\widehat{\mathcal{R}} = \Gamma[\beta\rho_{33}\widehat{P}_{11} + \beta\rho_{33}\widehat{P}_{22} - 2\rho_{33}\widehat{P}_{33} - (\rho_{31}\widehat{P}_{31} + \rho_{32}\widehat{P}_{32} + \mathrm{H.c.})]$$
$$- G \sum_{i,j=1,2,3} \rho_{ij}\widehat{P}_{ij} + \frac{G}{2}[\widehat{P}_{11} + \widehat{P}_{22}]. \tag{5}$$

For convenience, we assume that the upper state spontaneously relaxes with the total rate 2Γ. The relaxation rate of optical coherences (see below) can be denoted as $\Gamma_{eg} = \Gamma + G$ with G the time-of-flight relaxation rate attributed to the finite time of atom–field coherent interaction ($G \sim \tau^{-1}$, where τ is the mean time of the atomic flight through the area of the laser field). The branching ratio β is assumed to be equal for both arms of the Λ-scheme. The system of levels can be considered open by taking $\beta < 1$. $\widehat{P}_{nm}$ in (5) are the projection operators defined as $\widehat{P}_{nm} = |n\rangle \langle m|$.

Non-diagonal matrix elements ρ_{31}, ρ_{32} and Hermitian conjugate ones $\rho_{13} = \rho_{31}^*$, $\rho_{23} = \rho_{32}^*$ are optical coherences. In general, these elements can be expanded in series of spatial harmonics. In particular, for ρ_{31} and ρ_{32} in the RWA we have

$$\rho_{31}(z, t) = e^{-\mathrm{i}(\omega_1 t)} \sum_{n=-\infty}^{+\infty} \sum_{m=-\infty}^{+\infty} \rho_{31}^{(nm)} e^{\mathrm{i}(nk_1 + mk_2)z},$$
$$\rho_{32}(z, t) = e^{-\mathrm{i}(\omega_2 t)} \sum_{n=-\infty}^{+\infty} \sum_{m=-\infty}^{+\infty} \rho_{32}^{(nm)} e^{\mathrm{i}(nk_1 + mk_2)z}. \tag{6}$$

In fact, we take into account only a few harmonics from (6), and these lead to the following expansion for the other density matrix elements:

$$\rho_{12}(z, t) \approx e^{\mathrm{i}\Delta_{12}t}[\rho_{12}^{(+)}e^{\mathrm{i}k_{12}z} + \rho_{12}^{(-)}e^{-\mathrm{i}k_{12}z}] \tag{7}$$

with $\rho_{21} = \rho_{12}^*$, $\Delta_{12} = \omega_1 - \omega_2$, $k_{12} = k_1 - k_2$ and

$$\rho_{nn}(z) \approx \rho_{nn}^{(0)} + \rho_{nn}^{(+)}e^{2\mathrm{i}k_{12}z} + \rho_{nn}^{(-)}e^{-2\mathrm{i}k_{12}z}, \tag{8}$$

where $n = 1, 2, 3$. As long as we focus on the steady state of the atom, all spatial harmonics of the density matrix elements in (6)—(8) are assumed to be independent of time t.

As one can see, the populations of atomic levels contain the terms $\rho_{nn}^{(0)}$, which are not dependent on the z-coordinate. These elements can be treated as the space-averaged values of level populations. For instance, if there is only one traveling single-frequency light wave E_1 resonant to the $|1\rangle \rightarrow |3\rangle$ transition (see figure 10), the populations ρ_{11} and ρ_{33} will have only zero spatial harmonics $\rho_{11}^{(0)}$ and $\rho_{33}^{(0)}$. These populations only acquire high-order harmonics when additional light waves with different wavevectors are present in the cell. At the same time, we have another situation involving low-frequency coherences ρ_{12} and ρ_{21}. These matrix elements can be produced only by simultaneous action of two mutually coherent light beams with different wavevectors. Therefore, we have only space-dependent harmonics for the low-frequency coherences. An exception occurs when we consider the particular Λ-scheme with a degenerate ground state ($\mathcal{E}_1 = \mathcal{E}_2$). In such a case, two light
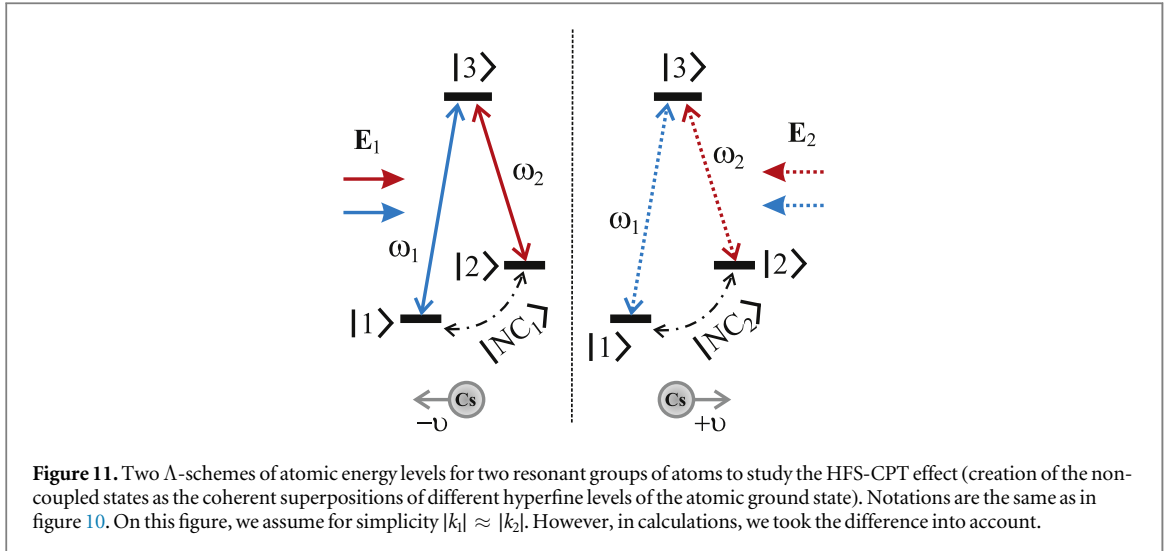
Figure 11. Two Λ-schemes of atomic energy levels for two resonant groups of atoms to study the HFS-CPT effect (creation of the non-coupled states as the coherent superpositions of different hyperfine levels of the atomic ground state). Notations are the same as in figure 10. On this figure, we assume for simplicity $|k_1| \approx |k_2|$. However, in calculations, we took the difference into account.

components with $\mathbf{k}_1 = \mathbf{k}_2$ produce coherences ρ_{12} and ρ_{21}, which do not depend on the z-coordinate. The last case is much easier to analyze theoretically (see section 3.2).

Optical coherences described in (6) can be excluded from the system of equation (2). Then, the final system includes only level populations $\rho_{nn}^{(0,\pm)}$ and low-frequency coherences $\rho_{12}^{(\pm)}$, $\rho_{21}^{(\pm)}$. For brevity, we put the final system of equations in the appendix.

In the experiments, the bichromatic light waves pass the cell in both directions (there and back) before reaching the photodetector. In this case, the absorbed power is proportional to the total fluorescence of the cell. On the other hand, the total fluorescence is proportional to the excited-state population averaged over the z-coordinate and velocity distribution of atoms in the gas. Therefore, we analyze the following expression as a spectroscopic signal

$$W(\Delta) = \langle \rho_{33}^{(0)} \rangle_v + \frac{2 \sin(k_{12}L)}{k_{12}L} \mathrm{Re}[\langle \rho_{33}^{(+)} \rangle_v \, \mathrm{e}^{ik_{12}L}], \qquad (9)$$

where L is the length of the vapor cell. The one-photon detuning $\Delta = \omega_1 - \omega_{31} = \omega_2 - \omega_{32}$ is assumed to be the same for both frequency components of the light field, and also the condition $\Delta = 0$ means that two counter-propagating waves are both in resonance with the atoms at rest. Angle brackets $\langle ... \rangle_v$ stand for averaging over the Maxwellian velocity distribution such as

$$\langle f(v) \rangle_v = \frac{1}{\sqrt{\pi}\, v_0} \int_{-\infty}^{+\infty} f(v) \mathrm{e}^{-v^2/v_0^2} \, \mathrm{d}v. \qquad (10)$$

Here $v_0 = \sqrt{2k_B T / m_0}$ is the most probable thermal velocity of an atom with mass m_0 in a gas with temperature T (k_B is the Boltzmann constant).

We note that, for convenience, spectra extracted from calculations in the theoretical section will be reported in terms of absorption and not transmission, as is done in the experimental section.

### 3.1. Hyperfine frequency splitting (HFS)-CPT states

In this subsection, we consider the case where the ground-state sublevels $|1\rangle$ and $|2\rangle$ arise from HF splitting of the ground state of the atom. For the ^{133}Cs atom, we have $|1\rangle \equiv |F = 3\rangle$, $|2\rangle \equiv |F = 4\rangle$, and $\Omega_{g,e} = 2\pi \nu_{g,e}$ are the frequency differences between hyperfine levels of the ground and excited states respectively. Magnetic sublevels are not considered in this subsection (see subsection 3.2). Before presenting the results of numerical calculations, it is useful to understand the reason for the formation of an absorption spike on a qualitative level.

In a first approach, we consider the situation where the Raman detuning $\Delta_R = 2\pi \delta_R = 0$ and the one-photon frequency detuning Δ is much larger than the natural linewidth Γ. In this case, each of the dual-frequency fields E_1 and E_2 interacts resonantly with a different velocity group of atoms, as shown in figure 11.

The field E_1 pumps atoms with velocity $-v$ into the non-coupled state $|NC_1\rangle$ while the field E_2 pumps those of velocity $+v$ into the non-coupled state $|NC_2\rangle$:

$$|NC_1\rangle = \frac{1}{\sqrt{2}}[|1\rangle - \mathrm{e}^{ik_{12}z}|2\rangle], \qquad (11)$$

$$|NC_2\rangle = \frac{1}{\sqrt{2}}[|1\rangle - \mathrm{e}^{-i(k_{12}z + \phi_{12} + 2\phi)}|2\rangle]. \qquad (12)$$
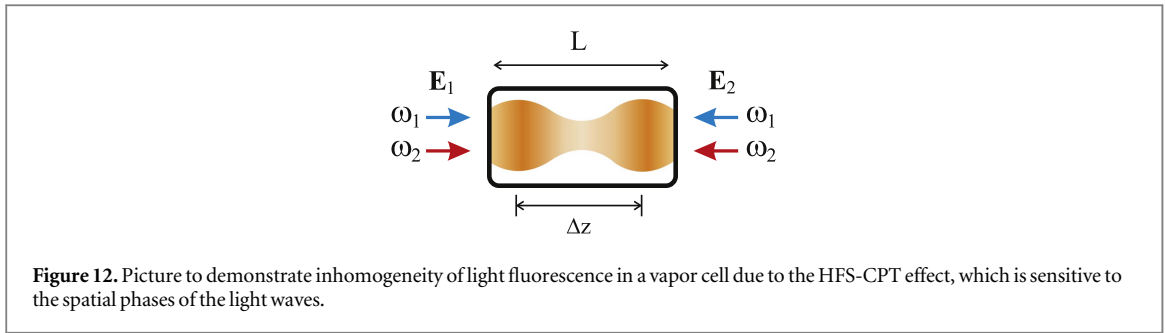
Figure 12. Picture to demonstrate inhomogeneity of light fluorescence in a vapor cell due to the HFS-CPT effect, which is sensitive to the spatial phases of the light waves.

Coherent population trapping occurs in these two velocity groups of atoms (see, for example, [31]). This means that atoms do not absorb any energy from the resonant light field. Therefore, absorption (fluorescence) of the vapor cell is low under the condition $\Delta \gg \Gamma$, explaining why atoms are in a so-called 'dark' state. In general, these states are different for two resonant groups of atoms since they interact with different light fields (E_1 or E_2). It is also worth noting that the mutual angle ϕ between linear polarizations of the counter-propagating dual-frequency waves and the relative spatial phase shift ϕ_{12} are additive contributions to the non-coupled state $|NC_2\rangle$ with $\theta = 2\phi + \phi_{12}$ (see the density matrix equations in the appendix). This means that the cell absorption depends on θ but not on these angles separately. In other words, by properly changing either ϕ_{12} or ϕ, we can get the same level of absorption.

Now, we need to consider the situation where $\Delta \sim \Gamma$ and where the fields E_1 and E_2 start to interact with the same atoms. In this configuration, two principal cases should be analyzed:

(i) $|NC_1\rangle$ and $|NC_2\rangle$ interfere destructively, i.e. $\langle NC_1|NC_2\rangle = 0$;

(ii) the 'competition' between $|NC_1\rangle$ and $|NC_2\rangle$ does not destroy the CPT effect, $\langle NC_1|NC_2\rangle = 1$.

In the first case, atoms start to absorb intensively and scatter energy from the light field since they are no longer in the dark state. From the expression (11), we can predict that this happens near the coordinates $z_{\max}$ satisfying the condition

$$k_{12} z_{\max} = \frac{\pi}{2} - \varphi - \frac{\varphi_{12}}{2} + \pi n, \tag{13}$$

with $n = 0, 1, \ldots$ The second condition (ii) is satisfied when

$$k_{12} z_{\min} = \pi n - \phi - \frac{\phi_{12}}{2}. \tag{14}$$

We can conclude that the fluorescence of the cell is inhomogeneous in space. There are areas with intense fluorescence and areas with low fluorescence (see a sketch in figure 12). These regions alternate with the period:

$$\Delta z = \frac{\pi}{|k_{12}|}. \tag{15}$$

It is interesting to note that the positions of maxima and minima of fluorescence depend on the phases ϕ, ϕ_{12} while the period Δz does not. This implies that for a sufficiently long cell, i.e. $L > \Delta z$, the level of total light-field absorption in the cell barely depends either on the angle between the linear polarizations or on the distance between the cell and the mirror 'M' (which produces the field E_2, see figure 1). By contrast, in the case when $L \ll \Delta z$, the fluorescence of the cell will be much more sensitive to the phases ϕ and ϕ_{12}. In the particular case of ^{133}Cs, we obtain from equation (15) that $\Delta z \approx 1.6$ cm. It should be noted that the qualitative analysis presented here and based on the formalism of non-coupled states is similar to the one previously reported in [37] for counter-propagating light waves with σ^+ and σ^- polarizations.

Let us support the analysis described above with absorption profiles calculated in several different cases. These profiles have been obtained by solving the density matrix equations whose explicit form can be found in the appendix. For our numerical calculations, we take slightly different Rabi frequencies of counter-propagating waves due to possible losses during the formation of the backward wave: $\Omega_{R1} = 1.5 \, \Gamma$, $\Omega_{R2} = 1.3 \, \Gamma$. The time-of-flight relaxation rate is $G = 5 \times 10^{-2} \, \Gamma$. The Doppler width is assumed to be $k v_0 = 94 \Gamma$. All these values approximately correspond to the experimental conditions. The absorption signal is integrated over the cell length.

A typical resonance is shown in figure 13. Its shape, if converted in transmission, is similar to the experimental one reported in figure 4. We see that the use of perpendicular polarizations allows us to reach a better contrast of the central peak. Nevertheless, a similar result can be obtained assuming $\phi = 0$ and $\phi_{12} = \pi$.
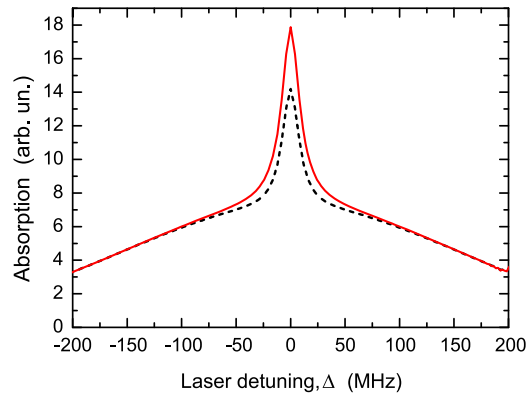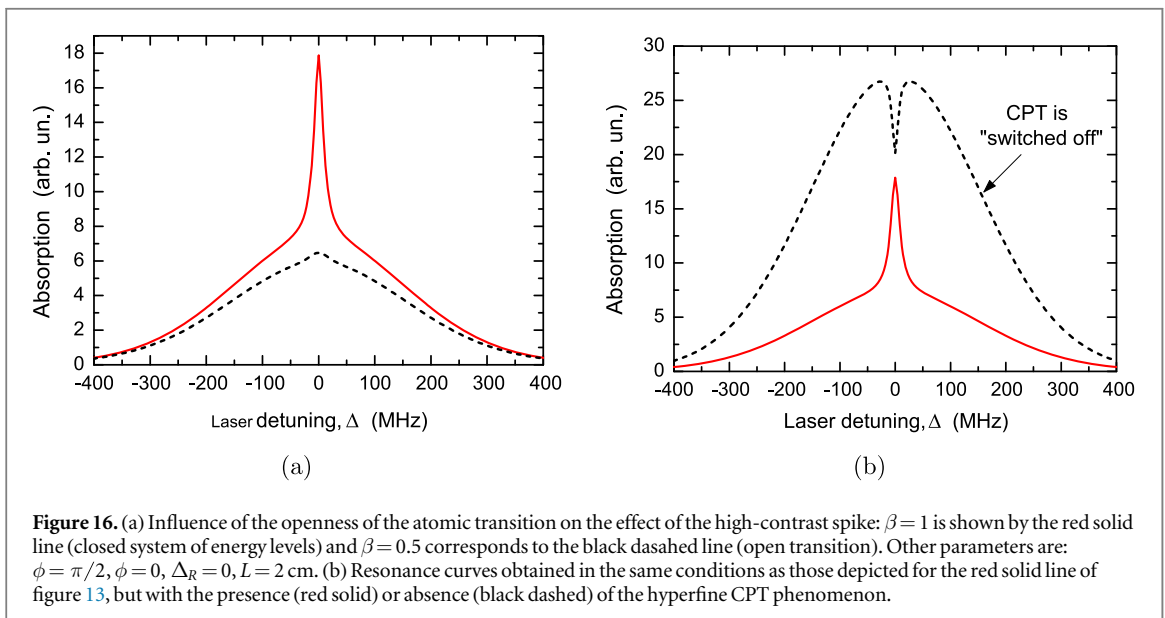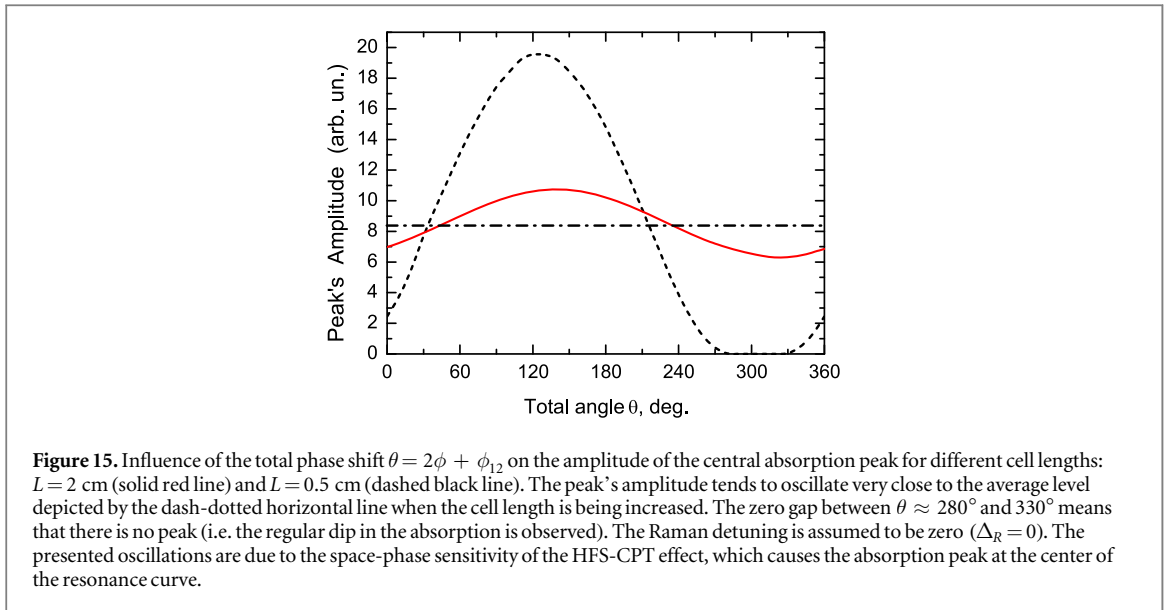
Figure 13. Absorption of the cell as a function of the one-photon detuning. The red solid curve is obtained for perpendicular polarizations ($\phi = \pi/2$), while the black dashed curve is obtained for parallel polarizations ($\phi = 0$). Other parameters are: $\Delta_R = 0$, $\beta = 1, L = 2$ cm, $\phi_{12} = 0$. The peak at the center can be observed due to the HFS-CPT effect.
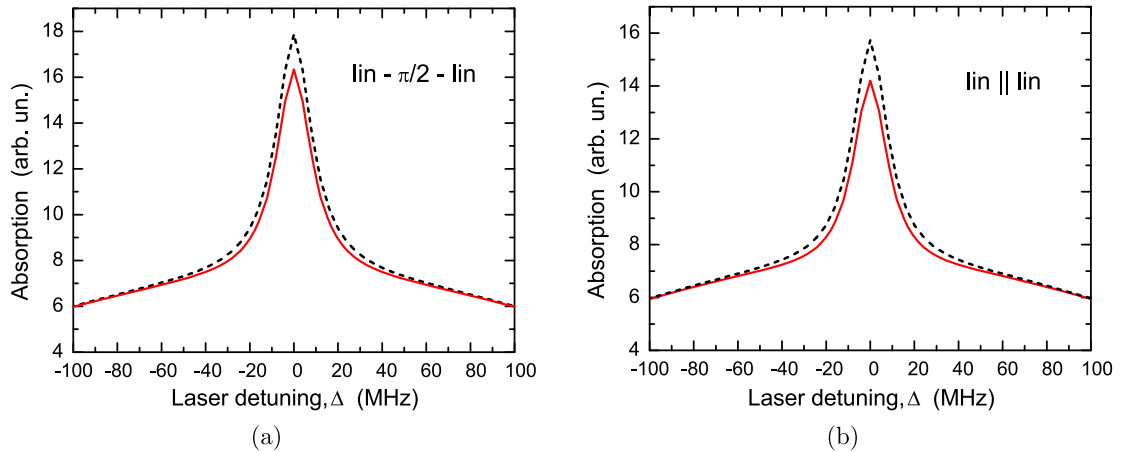
Figure 14. Illustration of the influence of cell length on the resonances in different polarization configurations: (a) perpendicular polarizations, (b) parallel polarizations. Solid red lines are obtained for a cell length $L = 2$ cm. Dashed black lines are obtained for $L = 5$ cm. Other parameters are: $\Delta_R = 0, \beta = 1, \phi_{12} = 0$. One can see that the HFS-CPT effect makes the central absorption peak sensitive to the light-field polarizations in the cases of short- or medium-length cells ($L \lesssim 2$ cm for cesium, compare amplitudes of the red-line resonances in parts (a) and (b)). At the same time, this sensitivity is absent for long cells, i.e. it is averaged along the length of a vapor cell. However, it should be emphasized that the total influence of the HFS-CPT effect on the creation of the central peak is not averaged along the cell, and the central peak caused by this effect can be observed even in the case of a long cell (see also figure 15).

Figure 14 shows the influence of the cell length on the strength of the central peak. In particular, if we take a long cell (compare black dashed curves in figures 14(a) and (b)), one can see that there is almost no difference between parallel and orthogonal light-wave polarizations. At the same time, using a medium-length cell having $L \sim \Delta z$ (as in our experiments, see solid lines of figure 14), the effect of sensitivity to the light polarizations can be visible. Thus, the amplitudes are ≈ 10 in figure 14(a) and ≈ 6 in figure 14(b). Figure 15 helps us to understand this sensitivity by showing the influence of the total phase shift $\theta = 2\phi + \phi_{12}$ on the amplitude of the central absorption spike for different cell lengths (2 cm and 0.5 cm). Variations of the spike amplitude are significantly higher for the short cell with $L = 0.5$ cm. For a sufficiently long cell ($L = 5$ cm and more), variations of the signal are very small and the spike amplitude is approximately constant. It tends to approach the average level presented in figure 15 as a dash-dotted horizontal line. This average level of absorption is described by the first term in equation (9).

It is interesting to note that we can observe the effect of the absorption peak for a very wide range of variations in the phase θ, while the effect is absent only for a short cell and for certain θ values in the range $280°$–$330°$ (see figure 15). This means that counter-propagating dual-frequency light waves can have common dark atomic states only in some relatively small regions along the cell, while the other regions show the effect of the absorption peak. For example, the interval $\approx 330 - 280 = 50° = 0.87$ rad in figure 15 for a short cell implies that the dark state remains common for both counter-propagating waves at the distance Δz, which can be estimated from the equation $2k_{12}\Delta z = 0.87$. For the conditions of figure 15, we immediately get

Figure 15. Influence of the total phase shift $\theta = 2\phi + \phi_{12}$ on the amplitude of the central absorption peak for different cell lengths: $L = 2$ cm (solid red line) and $L = 0.5$ cm (dashed black line). The peak's amplitude tends to oscillate very close to the average level depicted by the dash-dotted horizontal line when the cell length is being increased. The zero gap between $\theta \approx 280°$ and $330°$ means that there is no peak (i.e. the regular dip in the absorption is observed). The Raman detuning is assumed to be zero ($\Delta_R = 0$). The presented oscillations are due to the space-phase sensitivity of the HFS-CPT effect, which causes the absorption peak at the center of the resonance curve.

Figure 16. (a) Influence of the openness of the atomic transition on the effect of the high-contrast spike: $\beta = 1$ is shown by the red solid line (closed system of energy levels) and $\beta = 0.5$ corresponds to the black dashed line (open transition). Other parameters are: $\phi = \pi/2$, $\phi = 0$, $\Delta_R = 0$, $L = 2$ cm. (b) Resonance curves obtained in the same conditions as those depicted for the red solid line of figure 13, but with the presence (red solid) or absence (black dashed) of the hyperfine CPT phenomenon.

$\Delta z \approx 0.22$ cm. Thus, with a cell of length $L \leqslant 0.22$ cm, we should be able to totally destroy the effect of the absorption peak by a proper choice of the phase θ (for instance, by adjusting the mirror position).

Figure 16(a) describes the influence of the openness of the atomic transition (cases where the branching ratio is $\beta = 1$ or $\beta = 0.5$) on the high-contrast absorption effect. We clearly observe that, in the case of an open transition, the high-contrast spike almost disappears.

Figure 16(b) helps to clarify the physical origin of the formation of the central spike in the considered Λ-scheme. Figure 16(b) reflects the situation where the low-frequency coherences ρ_{12} and ρ_{21} are artificially 'switched off'. In this configuration, the creation of the HFS-CPT phenomenon is prohibited. One can see that there is no peak in the center of the absorption curve (black dashed line). On the contrary, a normal saturated-absorption resonance is observed. Secondly, the background level is found to be much higher when CPT is absent. Thus, from this figure and taking into account all other curves in this subsection, we can state that the central spike occurs because of the combination of a low level of background absorption at $\Delta \gg \Gamma$ and a 'normal' absorption level in the vicinity of a spectral line center at $\Delta \sim \Gamma$. This low background level is explained by the CPT phenomenon. Indeed, for $\Delta \gg \Gamma$, atoms from different velocity groups are pumped into the non-coupled states and do not scatter much light energy from the resonant field. For $\Delta \sim \Gamma$ the components of the light field start to interact with the same atoms, and non-coupled states can be destroyed (see the quantitative analysis in the previous subsection), leading to the increase in absorption. However, when CPT is artificially switched off, the Λ-scheme can be treated just as a pair of two-level schemes composed of the

Figure 17. Absorption as a function of the one-photon detuning in the dual-frequency case with a Raman detuning $\Delta_R = 0$ (red solid curve), $\Delta_R = 2\,\Gamma$ (blue dash-dotted curve) or $\Delta_R = 20\,\Gamma$ (dashed black curve). Other parameters are: $\phi = \pi/2$, $\beta = 1$, $L = 2$ cm.
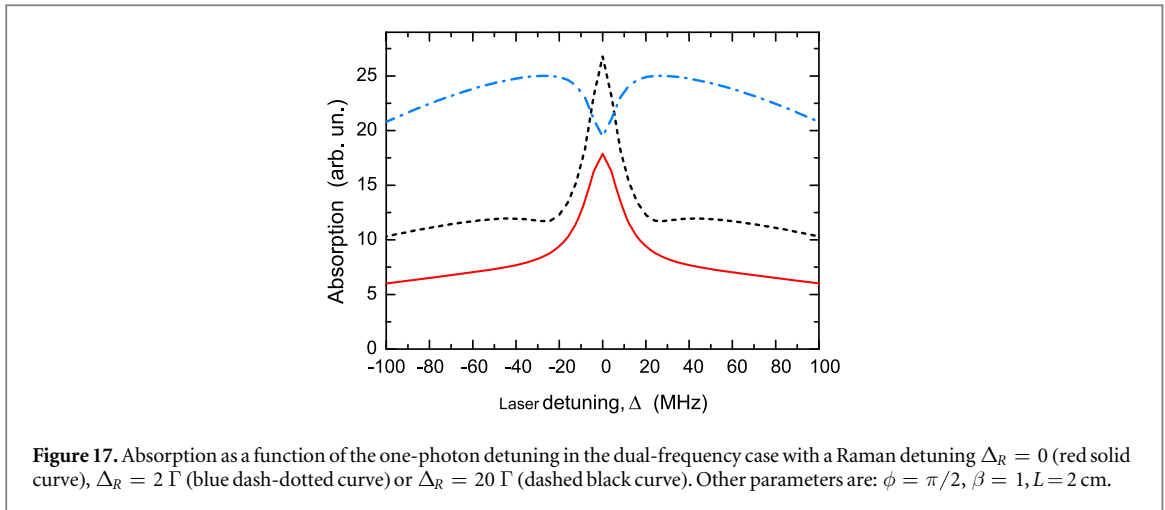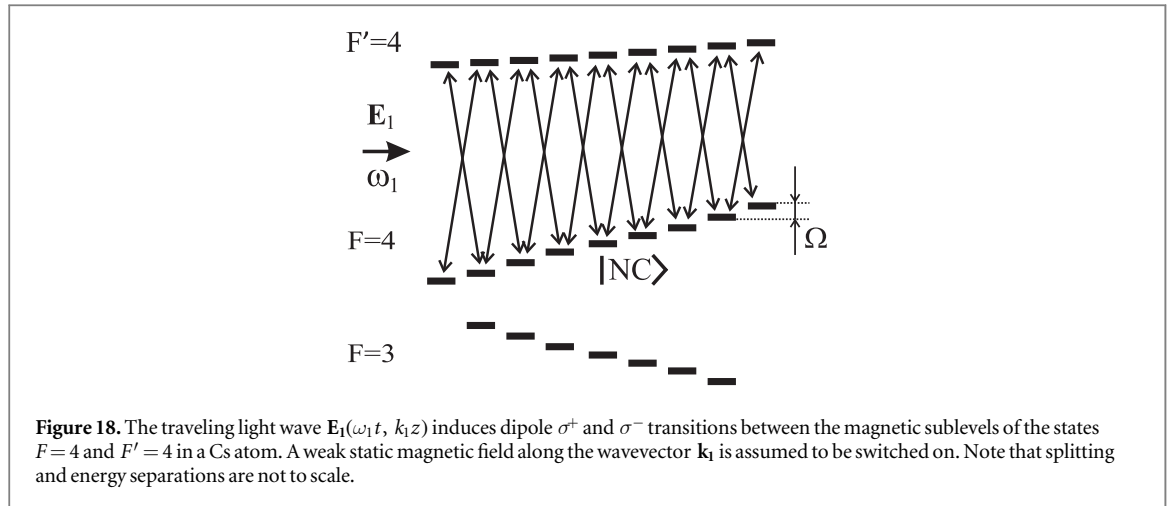
transitions $|1\rangle \leftrightarrow |3\rangle$ and $|2\rangle \leftrightarrow |3\rangle$ (see figure 10). Each of these systems leads to observation of a regular dip in saturated absorption when two counter-propagating waves act on the same atoms, i.e. in the center of the resonance curve (see the red profiles in figures 9(a), (b) and (d) where the HFS-CPT effect is absent). However, even if the HFS-CPT effect does not occur, an effect of the absorption peak can be observed for the other physical reasons considered in the following subsections. Such a case is represented by the black experimental curve in figure 9(d) where HFS-CPT is absent due to non-zero Raman detuning, but an absorption peak is observed. However, this peak is not as strong as in figure 9(c) where HFS-CPT takes place.

In conclusion of this subsection, we can say that the microwave HFS-CPT phenomenon involving different HFS sublevels of the ground state in ^{133}Cs can be a reason for the effect of a high-contrast spike observed in the experiments. Bearing that in mind, the resonance curve shown in figure 17 may appear surprising at first sight. Figure 17 shows the absorption when conditions are almost the same as those depicted for figure 13 (red solid profile) where a high-contrast resonance is observed. The difference is that we now consider a non-null Raman detuning Δ_R. Obviously, the spike effect disappears at $\Delta_R = 2\,\Gamma$ because CPT does not take place (see the blue dash-dotted curve in figure 17). Surprisingly, the central spike comes back for large Raman detunings ($\Delta_R = 20\,\Gamma$ for the black dashed curve in figure 17). In this case, microwave hyperfine CPT is absent. This results from the manifestation of another physical process, described in section 3.3, linked to some peculiarities of redistribution of populations of atomic energy levels due to the optical pumping process.

3.2. Zeeman CPT states

In the previous subsection, we have considered the formation of non-coupled states involving different levels of the HF doublet of the cesium ground state. However, another type of non-coupled state can be produced during the interaction of dual-frequency counter-propagating light waves with the energy structure of the D_1 line. This involves $|NC\rangle$ states embracing magnetic (Zeeman) sublevels of a single HF level [34]. For simplicity, figure 18 reflects the situation where the wave E_1 consists of a single frequency component ω_1. In this case, the wave can also pump the atoms to the non-coupled state consisting of many magnetic sublevels. The same frequency component (ω_1) of the counter-propagating wave E_2 (not shown in figure 18) can also lead to the CPT phenomenon on the state $F = 4$. Figure 18 plots the situation where the state $F' = 4$ is being excited. In this case, $|NC\rangle$ states can be produced only on a level with $F = 4$. If we consider the dual-frequency situation where both transitions 3–3' and 4–3' are nearly resonant, atoms can be driven to $|NC\rangle$ states on both HFS levels $F = 3, 4$. This driving scheme corresponds to the resonance observed on the right of figure 4.

In an analogous way to the previous section, counter-propagating beams interact with different velocity groups of atoms under the condition $\Delta \gg \Gamma$. Each of these groups can be pumped into the non-coupled state and demonstrates a low level of absorption. Near the center of the resonance ($\Delta \sim \Gamma$), the different non-coupled states attributed to different waves start to 'compete' with each other and the result depends in particular on the polarization configuration of the light waves. For simplicity, we consider only the CPT phenomenon that can take place on the HF level $F = 4$ (see figure 18). In this section, the situation is very similar to the one described in the previous subsection. Consequently, a spectroscopic model similar to that in the previous subsection (see figure 10) can be considered, but now taking $\Omega_g = 2\Omega$, where $\Omega = \mu_B g_2 B/\hbar$ is the Larmor frequency that characterizes the frequency splitting between magnetic sublevels of the ground level $F = 4$. B is the static magnetic field applied along the light wavevectors ($B||z$), μ_B is the Bohr magneton and $g_2 = 1/4$ is the Landé g-factor of the state $F = 4$. The Larmor frequency of the excited state can be written as

Figure 18. The traveling light wave $\mathbf{E_1}(\omega_1 t, k_1 z)$ induces dipole σ^+ and σ^- transitions between the magnetic sublevels of the states $F = 4$ and $F' = 4$ in a Cs atom. A weak static magnetic field along the wavevector $\mathbf{k_1}$ is assumed to be switched on. Note that splitting and energy separations are not to scale.

$(g_e/g_2)\Omega$ with $g_e = 1/12$ the g-factor of the state $F' = 4$. Landé factors of the ground HF levels have opposite signs, so that $g_1 = -g_2$.

While this spectroscopic model has many points in common with the previous one, it differs in some principal points. First, we consider the interaction of an atom with a light field having a single frequency component. Then, we can assume $\omega_1 = \omega_2 \equiv \omega$. This means also that $\mathbf{k_1} = -\mathbf{k_2} \equiv \mathbf{k}$, $\phi_{12} = 0$ and that the vapor fluorescence is homogenous along the cell. These conditions significantly simplify the calculations. Expression (6) can be simplified to

$$\rho_{31}(z, t) \approx e^{-i(\omega t)}[\rho_{31}^{(1)} e^{ikz} + \rho_{31}^{(2)} e^{-ikz}],$$
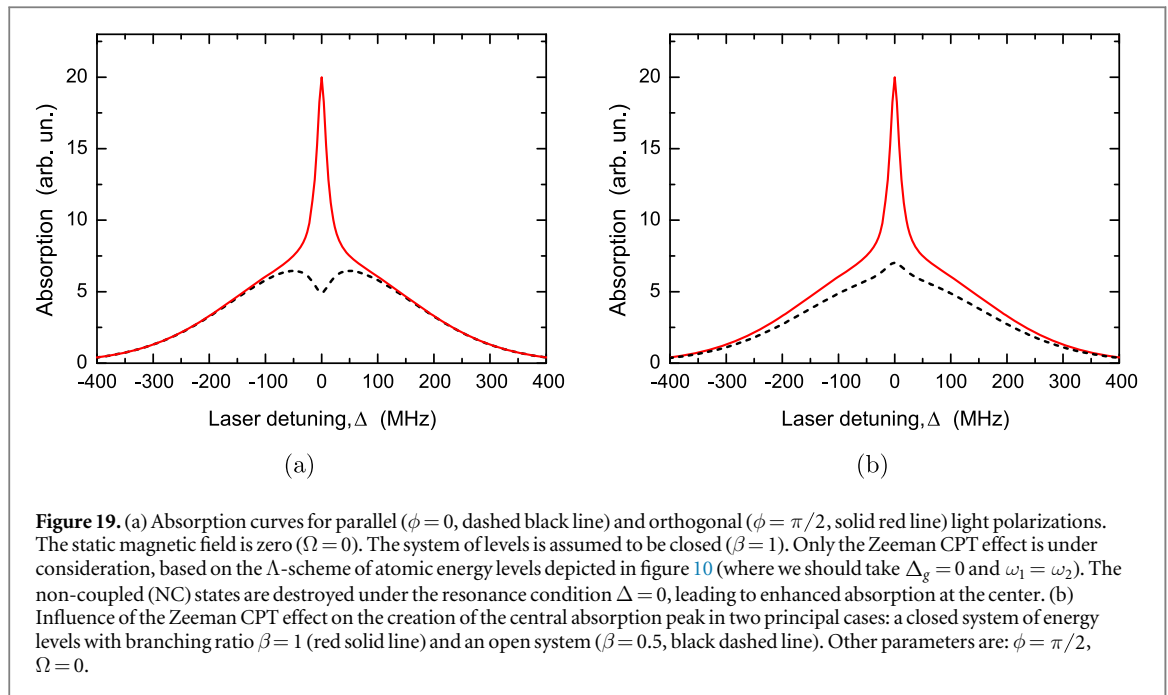$$\rho_{32}(z, t) \approx e^{-i(\omega t)}[\rho_{32}^{(1)} e^{ikz} + \rho_{32}^{(2)} e^{-ikz}], \tag{16}$$

Moreover, the other density matrix elements become homogeneous in space:

$$\rho_{12}(z, t) \approx \rho_{12}^{(0)}, \qquad \rho_{nn}(z) \approx \rho_{nn}^{(0)}. \tag{17}$$

Under these simplifications the final system of equations is much simpler than the system for the case of the HFS-CPT effect considered above (see also the appendix). However, for brevity, we do not provide the reader with this simplified system. Spatial homogeneity of the low-frequency coherence ρ_{12}, for instance, means that we omit very fast oscillation terms $\sim e^{\pm 2ikz}$ that have relatively little influence.

Let us analyze some figures. The spectroscopic signal can be described now by just the first term of expression (9). Figure 19(a) shows the resonance curves for parallel and orthogonal linear polarizations of the light waves. The physics of observed signals is similar to that described in the previous subsection. At the same time, the cell length now does not impact the strength of the effect (in the approximation of a small optical density). The central spike appears (red solid line) when non-coupled states created by both waves are orthogonal: $\langle NC_1|NC_2\rangle \approx 0$. This is the case for crossed polarizations (see figures 2(b) and 9(d)). The dip can be observed (dashed black line) when dark states $|NC_1\rangle$ and $|NC_2\rangle$ are close to each other (case of parallel polarizations, see figures 2(a) and 9(d). Note that a similar effect under a pump–probe regime was discussed in references [35, 38]. Figure 19(b) reflects the influence of the openness of the Λ-scheme. As for figure 16(a), we can here observe a dramatic suppression of the spike effect for an open transition. If creation of the CPT phenomenon is artificially 'switched off', we will get a similar result to figure 16(b).

Interesting transformations of the nonlinear spectroscopic signal can be observed by applying a gradual increase of the static magnetic field (see figure 20). One can see that the effect first disappears (for $\Omega > 0.5\ \Gamma$ under the considered conditions) but then comes back (for $\Omega > 2\ \Gamma$). This behavior is similar to that described in the previous section, where the two-photon detuning has been gradually increased. The behavior of the resonance in figure 20 between $\Omega = 0$ and $\Omega = 2\ \Gamma$ is easy to understand. In a small magnetic field, the spike formation is linked to the same reason as the one reported in figure 19(a) (red solid line). The CPT state, linked with the formation of a high-contrast spike, is destroyed with further increase in the magnetic field. We can estimate the interval of the Larmor frequency where the CPT state survives as $|\Omega| \leqslant \Omega_R^2/4\Gamma$ (from the power broadening condition). In conditions of figure 20, this means that the CPT state does not greatly influence the absorption profile when $|\Omega| \gg 0.5\ \Gamma$. Therefore, the usual dip in saturated absorption is observed in figures 20(d) and (e), as in figure 2(b) at high magnetic field. This situation is similar to that in figure 16(b) where the CPT is 'switched off'. However, with a further increase in the magnetic field, the spike can be observed again. The reason for this behavior is the same as for figure 17, where a large Raman detuning ($\Delta_R \neq 0$) was considered. Here, the Larmor frequency Ω plays the role of this Raman detuning. The creation of the high-

Figure 19. (a) Absorption curves for parallel ($\phi = 0$, dashed black line) and orthogonal ($\phi = \pi/2$, solid red line) light polarizations. The static magnetic field is zero ($\Omega = 0$). The system of levels is assumed to be closed ($\beta = 1$). Only the Zeeman CPT effect is under consideration, based on the Λ-scheme of atomic energy levels depicted in figure 10 (where we should take $\Delta_g = 0$ and $\omega_1 = \omega_2$). The non-coupled (NC) states are destroyed under the resonance condition $\Delta = 0$, leading to enhanced absorption at the center. (b) Influence of the Zeeman CPT effect on the creation of the central absorption peak in two principal cases: a closed system of energy levels with branching ratio $\beta = 1$ (red solid line) and an open system ($\beta = 0.5$, black dashed line). Other parameters are: $\phi = \pi/2$, $\Omega = 0$.
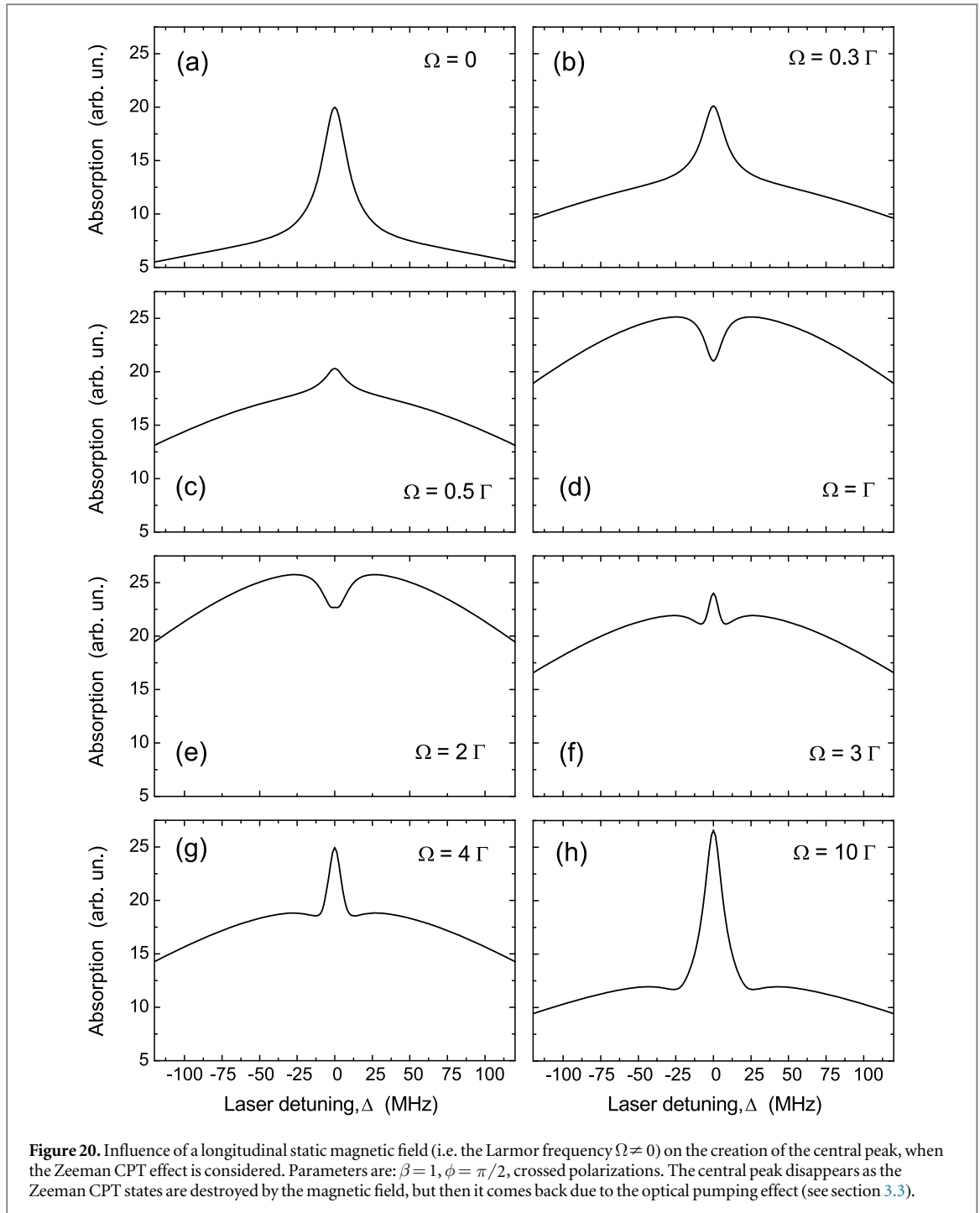
contrast spike under the condition $\Omega \gg \Gamma$ is due to peculiarities of the optical pumping process. This aspect is discussed in the next subsection.

3.3. Peculiarities of optical pumping

In this subsection, we discuss the last physical phenomenon that can contribute to the observation of the high-absorption dip in the center of the absorption profile. This effect can also be understood with the help of a Λ-scheme. As mentioned above, some peculiarities of the optical pumping process can lead to the observation of the peak in cases of figure 17 (black dashed line) or figures 20(f)–(h).
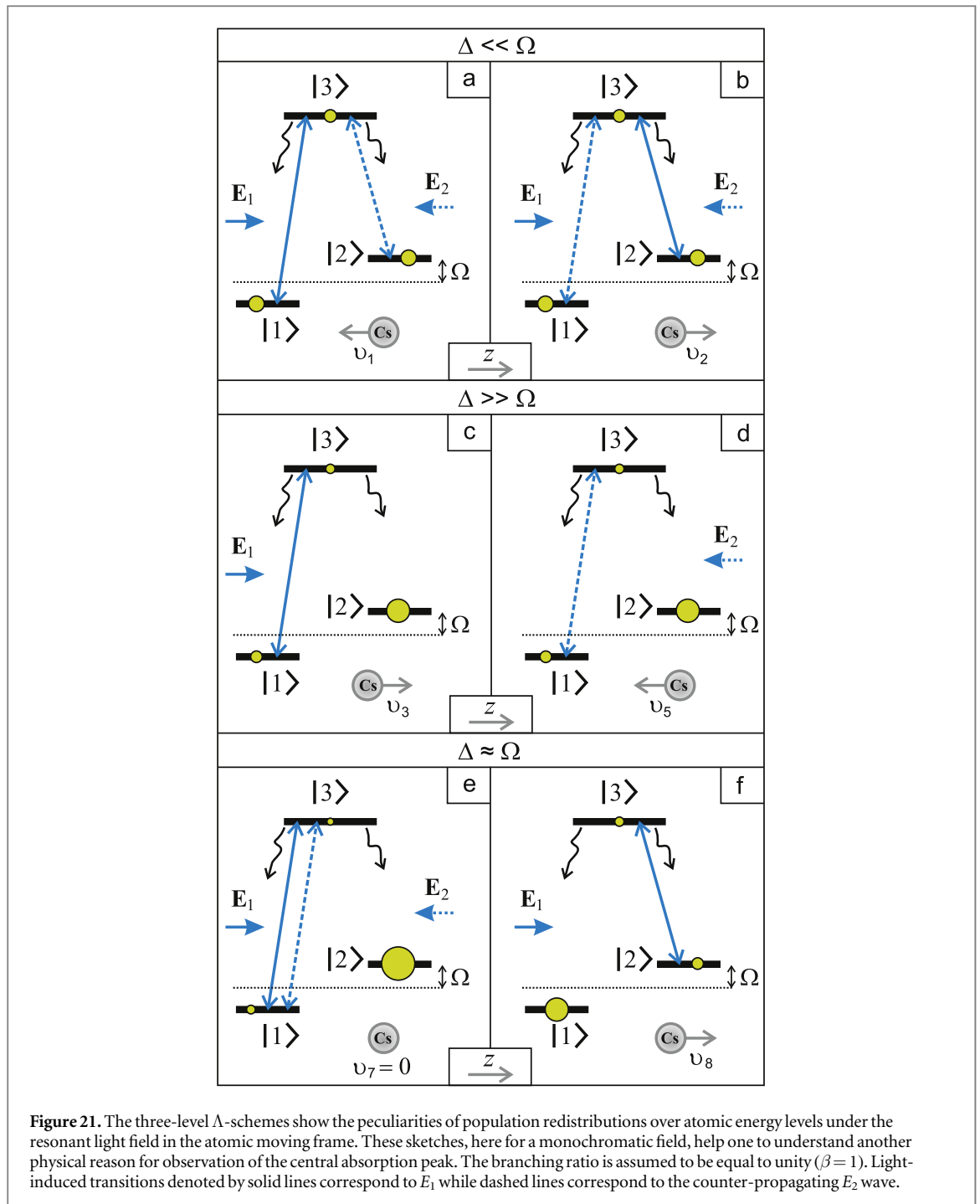
Let us consider the case of the formation of the peak, in the monochromatic case with crossed polarizations, when the Larmor frequency is large enough to destroy the influence of the CPT phenomenon. We also assume that Ω is larger than the natural linewidth of the transition. In other words, we focus on the case of $\Omega = 10\,\Gamma$ where the peak effect is strong enough (see figure 20(h)). Figures 21(a)–(f) are given to describe qualitatively the physical reason for the formation of the peak. We assume Δ to be positive as well as the Larmor frequency Ω (i.e., we consider the right part of the curve in figure 20(h)). When the vapor is being irradiated by a laser field, only specific velocity groups of atoms are excited due to the Doppler shift. Therefore, we will consider here the contributions from different resonant velocity groups from different cases of frequency detuning. In a first approach, let us compare the cases where $\Gamma \sim \Delta \ll \Omega$ (central part of the absorption curve, see figure 21) and $\Delta \gg \Omega$ (background level). In the former case, there are two symmetrical resonant groups with velocities $v_{1,2} \approx \mp \Omega/k$ ($\Delta \ll \Omega$). Each group interacts simultaneously with the $\sigma^{+(-)}$ polarization component of one wave and with $\sigma^{-(+)}$ of the other (counter-propagating) wave. This means that there is a *closed* system of levels, having the following main features: (1) both ground Zeeman sublevels interact with the field, (2) populations of these sublevels are almost equal, (3) the upper state is also populated and the fluorescence (absorption) is significant. It should be noted that there are CPT-like states that are produced by the counter-propagating waves in this case; however, these states oscillate very fast in space with $\exp[\pm 2ikz]$. Because of this, only the small number of atoms in a gas that have almost zero z-component of velocity can be pumped into such a CPT state. The remaining resonant atoms (the overwhelming majority) cannot follow these spatial phase oscillations adiabatically . Moreover, the second reason why the mentioned zero-velocity group of atoms does not affect the observed signal is that this effect ($\sim \exp[\pm 2ikz]$) is almost averaged along the length of the cell, because for a regular cell we have condition $kL \gg 2k\lambda$ (we do not consider a micrometer-length cell here). These rapid spatial variations are the sense of difference between this kind of dark state and the dark states considered in section 3.1, where two CPT states were created only by the wave E_1 or E_2 and oscillated in space much more slowly (according to the varying term $\exp[\pm ik_{12}z]$).

In the regime $\Delta \gg \Omega$, there are two pairs of resonant groups of atoms—each pair is resonant only with the E_1 or E_2 wave. The central velocities of these groups are $v_{3,4} = (\Delta \pm \Omega)/k$ for the E_1 wave and $v_{5,6} = -(\Delta \pm \Omega)/k$ for the E_2 wave. For brevity, figures 21(c) and (d) reflect the cases for only two of these groups. The main difference between this regime and the one considered above ($\Gamma \sim \Delta \ll \Omega$) is that we have here four

Figure 20. Influence of a longitudinal static magnetic field (i.e. the Larmor frequency $\Omega \neq 0$) on the creation of the central peak, when the Zeeman CPT effect is considered. Parameters are: $\beta = 1$, $\phi = \pi/2$, crossed polarizations. The central peak disappears as the Zeeman CPT states are destroyed by the magnetic field, but then it comes back due to the optical pumping effect (see section 3.3).

independent resonant groups of atoms, which are described by the corresponding Λ-schemes. The main feature of each of these schemes is that they induce 'trap' states, which accumulate a major part of the atomic population. For example, in the case of figure 21(c), this trap state is $|2\rangle$. We can say that this system is effectively *open* because atoms being trapped in the state $|2\rangle$ no longer interact with the field. This leads to a large decrease in the excited-state population and the absorption level correspondingly. Therefore, one can observe a strong absorption (a peak) in the center of the resonance and a small background level. This situation is similar to the cases depicted in figures 13 or 19(a) (solid red curves) where the $|NC\rangle$ states played the role of the trap state for large frequency detunings, and these $|NC\rangle$ trap states were disrupted and thus absent in the center of the absorption curves where $\Delta = 0$.

An interesting feature to note is the small dip at the base of the peaks in figures 20(f)–(h). This is explained by Λ-schemes depicted in figures 21(e) and (f). When $\Delta \approx \Omega$, there is a special resonant group of atoms with zero z-projection ($v_z \approx 0$) where two waves act on the same arm of the Λ-scheme (figure 21(e)). In this case, the trap state $|2\rangle$ is better optically pumped than in the situation where only one resonant wave is involved (figures 21(c),
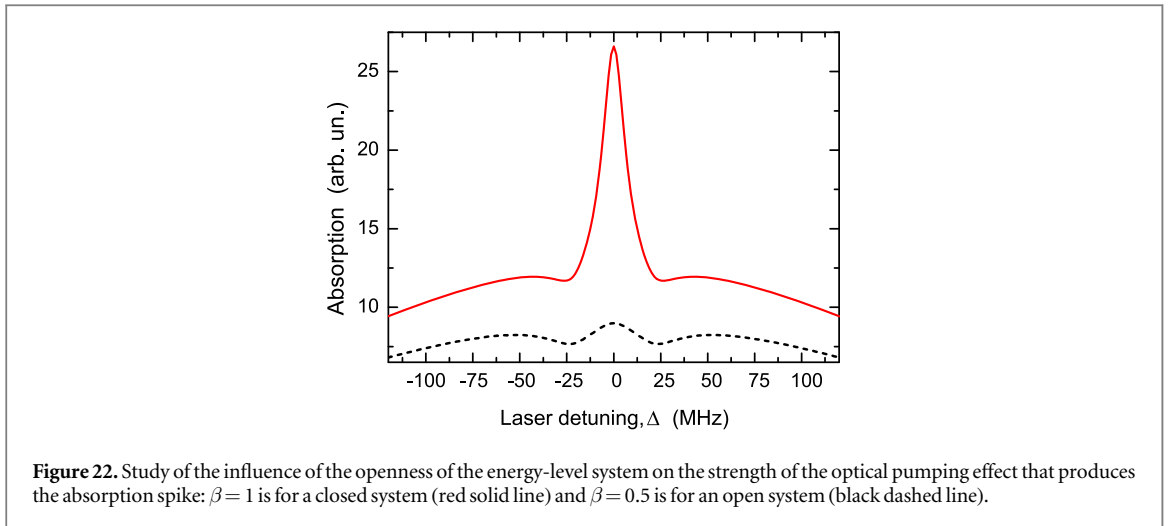
Figure 21. The three-level Λ-schemes show the peculiarities of population redistributions over atomic energy levels under the resonant light field in the atomic moving frame. These sketches, here for a monochromatic field, help one to understand another physical reason for observation of the central absorption peak. The branching ratio is assumed to be equal to unity ($\beta = 1$). Light-induced transitions denoted by solid lines correspond to E_1 while dashed lines correspond to the counter-propagating E_2 wave.

(d)). This means that the upper state suffers from additional reduction of the population and the fluorescence decreases.

The optical pumping effect that produces the absorption spike considered here is sensitive to the branching ratio. This sensitivity is demonstrated in figure 22. With a slightly open system, the peak does not disappear but its amplitude is much smaller than for a closed system. In a real experiment with ^{133}Cs, the peak-producing optical pumping effect described here can be realized on its own by utilizing a combination of the two previously discussed techniques: by using two independent laser sources (or large Raman detuning Δ_R, to kill the HFS-CPT effect) together with a non-zero longitudinal magnetic field B (to 'kill' the Zeeman-CPT effect). We should note that a similar effect connected with the optical pumping process was also described with potassium atoms [39].

3.4. Discussions

Let us compare the results of the experiments (section 2) and the theoretical analysis described in sections 3.1–3.3. First, we are interested in the dual-frequency regime of atom–field interaction. Figure 2(a) reports the usual saturated-absorption resonance as a reduction in absorption of the vapour cell near $\Delta = 0$. By contrast, in the
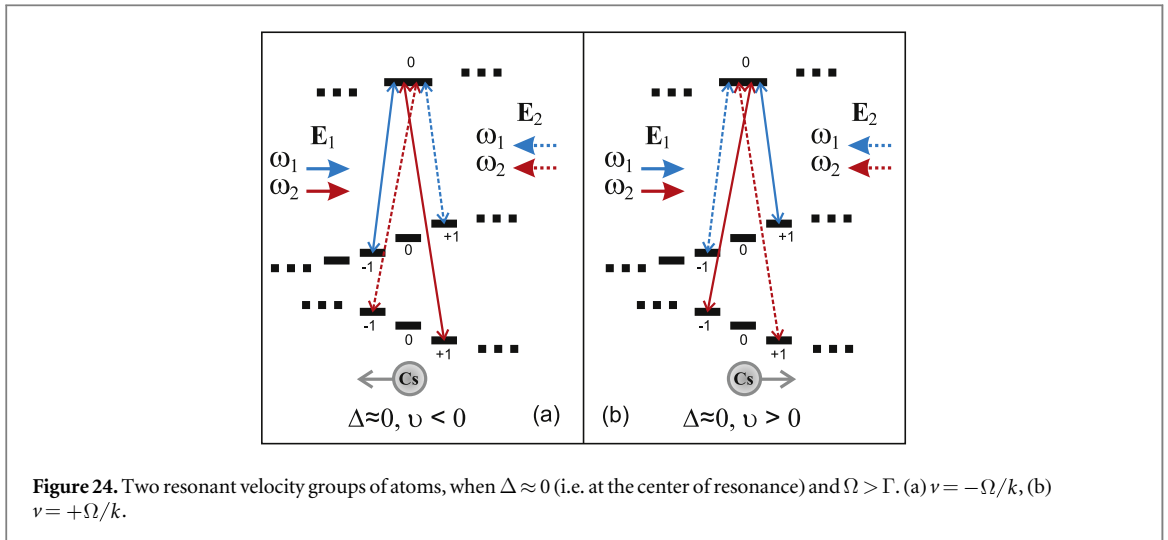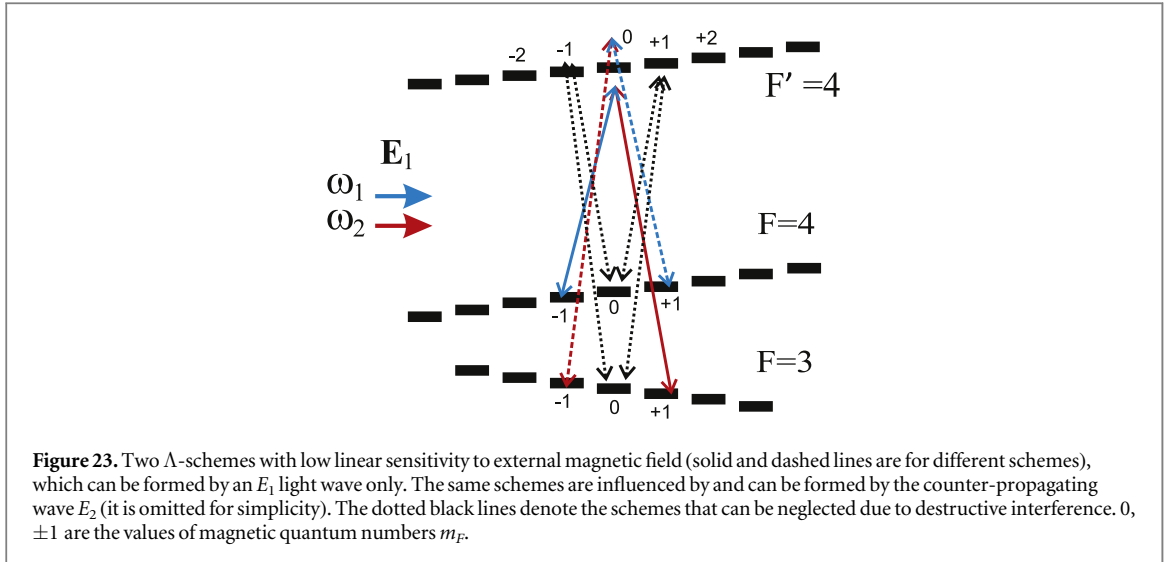
Figure 22. Study of the influence of the openness of the energy-level system on the strength of the optical pumping effect that produces the absorption spike: $\beta = 1$ is for a closed system (red solid line) and $\beta = 0.5$ is for an open system (black dashed line).

dual-frequency regime (figure 4), a high-contrast enhanced-absorption peak is detected when both HF ground states ($F = 3$ and $F = 4$) are excited by the counter-propagating waves. We have already described several possible physical reasons underlying this effect. As mentioned above, we focus here on the spike that corresponds to the interaction between the light field and the $F' = 4$ upper state. Similar explanations can be provided for the adjacent spike.

When the static magnetic field is close to zero, two main physical reasons can contribute to the creation of the absorption peak. Both are manifestations of the phenomenon of coherent population trapping. We distinguish the HFS-CPT and the Zeeman-CPT (see sections 3.1 and 3.2, respectively). Both effects can lead to a reduced absorption over the whole Doppler profile (see an example in figure 16(b)).

The Zeeman-CPT effect leads to a regular SAR dip at the center of the resonance in the case of parallel polarizations of the counter-propagating waves since the $|NC\rangle$ states generated by the fields are compatible, and to an enhanced absorption in the case of perpendicular polarization since the $|NC\rangle$ states are, in that case, orthogonal (see figures 19(a) and 9(d)). At the same time, even the Zeeman-CPT effect may not result in observation of the effect of the absorption peak if optical transition is essentially open (see the black side resonance in figures 9(a) and (b)). It should also be noted that, unlike the HFS-CPT effect, the Zeeman-CPT effect is independent of the cell length since the two fields responsible for manifestation of the effect have the same k-vectors.

The HFS-CPT effect can result in an increased-transmission or increased-absorption resonance for the parallel as well as the perpendicular polarizations. The sign (dip or peak) of the contribution of the HFS-CPT process depends on the cell length L and on the position of the mirror M (figure 1), i.e. the phase shift ϕ_{12} (see figure 15). For a cell of intermediate length (as in our experiments, $L = 2$ cm), both effects have the same sign for the perpendicular polarization of the light waves and contribute to the creation of the central spike. However, when the light-wave polarizations are parallel, the creation of the absorption peak can be caused only by the HFS-CPT effect (see figures 19(a) and 9(c)). This explains why the peak amplitude is smaller in the case of parallel versus orthogonal polarization (see figures 6(a) and 5(a) for $B = 0$). Note that both effects, HFS-CPT and Zeeman-CPT, take place in figure 9(c), while only Zeeman-CPT occurs in figures 9(a), (b) and (d) because HFS-CPT is eliminated by the non-zero Raman detuning. The width of HFS-CPT resonances is about 300 kHz, as measured in section 2.3.3. This means that the Raman detuning $\Delta_R = 2\pi \times 1$ MHz of figure 9(d) is large enough to destroy the influence of this effect on the resonance curves. The theoretical calculation reported in figure 17 (blue dash-dotted curve) also demonstrates the destruction of the HFS-CPT effect under a non-zero Raman detuning ($2\,\Gamma$ for the presented figure).

The reduction in the spike amplitude in the presence of a magnetic field is also obvious (see figure 5(a)). Indeed, in the case of ^{133}Cs, the splitting of ground-state Zeeman sublevels (of the $F = 3$ or $F = 4$ level) follows the law $|\Omega| = 2\pi \times 0.35$ MHz G^{-1} (this law can be easily calculated or revealed directly from figure 8 because the frequency interval between two adjacent transmission peaks corresponds to $2\,\Omega$). This means that, when a non-zero magnetic field exists in the cell, the non-coupled states $|NC\rangle$, which are certain superpositions of the magnetic sublevels m_F of one ground level ($F = 3$ or $F = 4$, see figure 18), cannot be created (see section 3.2). The critical value of the magnetic field is about 300–400 mG as shown in figure 3(b). Therefore, the 'Zeeman-CPT' effect does not contribute to the peak formation under the condition $\Omega > \Delta_{CPT}$, with Δ_{CPT} the width of the Zeeman-CPT resonance (see also figure 20(d) where the CPT resonance vanishes under $\Omega \sim \Gamma$). In other

Figure 23. Two Λ-schemes with low linear sensitivity to external magnetic field (solid and dashed lines are for different schemes), which can be formed by an E_1 light wave only. The same schemes are influenced by and can be formed by the counter-propagating wave E_2 (it is omitted for simplicity). The dotted black lines denote the schemes that can be neglected due to destructive interference. 0, ±1 are the values of magnetic quantum numbers m_F.

Figure 24. Two resonant velocity groups of atoms, when $\Delta \approx 0$ (i.e. at the center of resonance) and $\Omega > \Gamma$. (a) $v = -\Omega/k$, (b) $v = +\Omega/k$.

words, Λ-schemes with two ground magnetic sublevels belonging to a single HFS ground state are very sensitive to the external magnetic field.

At the same time, one could expect that the HFS-CPT effect can contribute to the creation of the absorption peak even in the presence of a non-null magnetic field. Indeed, figure 23 (solid and dashed red and blue arrows) shows that there are two Λ-schemes, almost insensitive to the magnetic field. These schemes embrace the common upper sublevel $|F' = 4, m_{F'} = 0\rangle$ and two pairs of ground-state magnetic sublevels: $\{|F = 3, m_F = +1\rangle$ and $|F = 4, m_F = -1\rangle\}$ or $\{|F = 3, m_F = -1\rangle$ and $|F = 4, m_F = +1\rangle\}$. The linear sensitivity of these schemes to the magnetic field is only due to the nuclear magnetic momentum (e.g., see [40–42]). Based on the figure, one could expect that the absorption peak would also survive in a moderate magnetic field. Unfortunately, in the case of ^{133}Cs, we cannot distinguish single Λ-schemes in moderate magnetic fields ($B \sim 1$ G), which could provide a pure and strong HFS-CPT effect. The fact is that, when $\Omega \lesssim \Gamma$, there are additional light-induced σ-transitions in the atom besides those shown in figure 23. For example, the transition $\{|F = 3, m_F = +1\rangle \to |F' = 4, m_F = +2\rangle\}$ is also permitted. This transition destroys the CPT state as the superposition of $\{|F = 3, m_F = -1\rangle$ and $|F = 4, m_F = +1\rangle\}$ sublevels.

On the other hand, we could expect that the single Λ-schemes would be distinguished with a further increase in the magnetic field ($\Omega > \Gamma$), when transitions like $\{|F = 3, m_F = +1\rangle \to |F' = 4, m_F = +2\rangle\}$ become out of the one-photon resonance and the HFS-CPT effect would occur. Increasing the magnetic field also means that two light waves resonantly interact with atoms having non-zero velocities (figure 24), in contrast to what we have for small magnetic field values (figure 23). Atoms in each of the two resonant velocity groups interact with both counter-propagating waves, and the pure Λ-schemes can be created. However, the fact is that these Λ-schemes are independent of each other, i.e. each of these schemes is driven only by one wave (E_1 or E_2, see figure 24). Therefore, the waves almost do not 'feel' each other under the condition $\Omega > \Gamma$ and there is no reason for the

creation of the absorption peak again. All the above explains why the absorption peak does not survive as the magnetic field in the experiments is increased (for instance, see figure 5(a)). Nevertheless, with a further increase in the magnetic field, the peak comes back ($B \approx 2$ G under the conditions of our experiments, see figures 5(a), 6(a)). This happens due to the 'pumping' effect described in the previous subsection. However, the peak amplitude is not as large as in the case of zero magnetic field because of the considerable openness of the relevant atomic energy levels (especially under the condition $\Omega > \Gamma$), which harms the effect of the absorption peak as shown above (see figure 22). Therefore, when $B > 1$ G, the absorption peak can be observed, but its amplitude is much smaller than in zero magnetic field.

In principle, two other Λ-schemes are insensitive to the magnetic field (dotted black lines in figure 23). These schemes have common ground-state magnetic sublevels $|F = 3,\ m_F = 0\rangle$ and $|F = 4,\ m_F = 0\rangle$ and are totally insensitive to the linear Zeeman shift (in the sense of a two-photon resonance). However, it can be shown that the $|\text{NC}\rangle$ states cannot be produced in the case of parallel or orthogonally polarized counter-propagating waves as long as the atom is excited by the two-frequency laser field. Indeed, it is enough to consider just one of the two waves, for example the E_1 wave. If two frequency components ($\omega_{1,2}$) have parallel linear polarizations, the dark state between $|F = 3,\ m_F = 0\rangle$ and $|F = 4,\ m_F = 0\rangle$ cannot be created due to the relative phases of the Clebsch–Gordan coefficients. This feature has been mentioned and studied in many papers, so we do not pay much attention to it here (e.g., see [33, 43–45]). Therefore, the Λ-schemes shown in figure 23 as the dotted black lines can be omitted from our consideration.

4. Conclusions

We have reported a detailed experimental study on Doppler-free spectroscopy on the Cs D$_1$ line with the use of a dual-frequency optical field. We demonstrated under appropriate conditions the possibility to detect high-contrast natural-linewidth resonances appearing as a sudden increased-absorption spike in the center of the Doppler profile. The impact of several experimental parameters on the shape, sign and amplitude of this resonance was investigated, including the polarizations of the light waves, the static magnetic field, and laser or Raman frequency detunings. These experimental results were supported by a detailed theoretical analysis, which revealed the effect to be really many-sided. Several simplified spectroscopic models were proposed to explain the results of the experiments due to the variety of physical effects involved into the creation of the absorption peak. All these models are based on a Λ-scheme of atomic energy levels. It was highlighted that the high-contrast resonance spike appearing in the bottom of the absorption profile is mainly attributed to three physical phenomena—microwave dark-state coherences ('HFS-CPT' effect), dark states composed of coherent superpositions of Zeeman sublevels of the same hyperfine level ('Zeeman-CPT' effect) and optical pumping processes. In the general case, all these physical reasons contribute constructively and lead to the natural-width bright resonance observed in the absorption of the vapour cell. Experimental observations and theoretical descriptions reported in this article could be of great interest in various domains of fundamental and applied physics including high-resolution laser spectroscopy, laser frequency stabilization, quantum optics and metrology.

Acknowledgments

Appendix

Numerical calculations of absorption curves presented in subsection 3.1 are based on the following system of equations for density matrix elements. This system has been derived by substituting (3)–(8) into the master equation (2).

$$(G + 2\Gamma_{eg}[S_{11}^{(-)} + S_{21}^{(+)}])\rho_{11}^{(0)} - (\beta\Gamma + 2\Gamma_{eg}[S_{11}^{(-)} + S_{21}^{(+)}])\rho_{33}^{(0)}$$

$$+\Omega_{R1}^2 L_1^{(-)}\rho_{12}^{(-)} + \Omega_{R20}^2 L_1^{(+)}e^{-i\theta}\rho_{21}^{(+)} + \Omega_{R1}^2 L_1^{(-)*}\rho_{21}^{(+)} + \Omega_{R20}^2 L_1^{(+)*}e^{i\theta}\rho_{21}^{(-)} = \frac{G}{2}, \tag{A1}$$

$$(G + 2\Gamma_{eg}[S_{12}^{(-)} + S_{22}^{(+)}])\rho_{22}^{(0)} - (\beta\Gamma + 2\Gamma_{eg}[S_{12}^{(-)} + S_{22}^{(+)}])\rho_{33}^{(0)}$$

$$+\Omega_{R1}^2 L_2^{(-)*}\rho_{12}^{(-)} + \Omega_{R20}^2 L_2^{(+)*}e^{-i\theta}\rho_{12}^{(+)}\Omega_{R1}^2 L_2^{(-)}\rho_{21}^{(+)} + \Omega_{R20}^2 L_2^{(+)}e^{i\theta}\rho_{21}^{(-)} = \frac{G}{2}, \tag{A2}$$

$$(G + \Omega_{R1}^2 M_{12}^{(+)} + \Omega_{R20}^2 M_{12}^{(-)*} + 2ik_{12}v)\rho_{11}^{(+)} - (\beta\Gamma + \Omega_{R1}^2 M_{12}^{(+)} + \Omega_{R20}^2 M_{12}^{(-)*})\rho_{33}^{(+)}$$

$$+\Omega_{R1}^2 M_{12}^{(+)}\rho_{12}^{(+)} + \Omega_{R20}^2 M_{12}^{(-)*}e^{i\theta}\rho_{21}^{(+)} = 0. \tag{A3}$$

Taking into account the connection $\rho_{11}^{(-)} = \rho_{11}^{(+)*}$, we immediately get

$$(G + \Omega_{R1}^2 M_{12}^{(+)*} + \Omega_{R20}^2 M_{12}^{(-)} - 2ik_{12}v)\rho_{11}^{(-)} - (\beta\Gamma + \Omega_{R1}^2 M_{12}^{(+)*} + \Omega_{R20}^2 M_{12}^{(-)})\rho_{33}^{(-)}$$

$$+\Omega_{R1}^2 M_{12}^{(+)*}\rho_{21}^{(-)} + \Omega_{R20}^2 M_{12}^{(-)}e^{-i\theta}\rho_{12}^{(-)} = 0. \tag{A4}$$

For harmonics $\rho_{22}^{(\pm)}$ we have

$$(G + \Omega_{R1}^2 M_{21}^{(+)*} + \Omega_{R20}^2 M_{21}^{(-)} + 2ik_{12}v)\rho_{22}^{(+)} - (\beta\Gamma + \Omega_{R1}^2 M_{21}^{(+)*} + \Omega_{R20}^2 M_{21}^{(-)})\rho_{33}^{(+)}$$

$$+\Omega_{R1}^2 M_{21}^{(+)*}\rho_{12}^{(+)} + \Omega_{R20}^2 M_{21}^{(-)}e^{i\theta}\rho_{21}^{(+)} = 0, \tag{A5}$$

$$(G + \Omega_{R1}^2 M_{21}^{(+)} + \Omega_{R20}^2 M_{21}^{(-)*} - 2ik_{12}v)\rho_{22}^{(-)} - (\beta\Gamma + \Omega_{R1}^2 M_{21}^{(+)} + \Omega_{R20}^2 M_{21}^{(-)*})\rho_{33}^{(-)}$$

$$+\Omega_{R1}^2 M_{21}^{(+)}\rho_{21}^{(-)} + \Omega_{R20}^2 M_{21}^{(-)*}e^{-i\theta}\rho_{12}^{(-)} = 0. \tag{A6}$$

For low-frequency coherences

$$\{G + \Omega_{R1}^2[M_{21}^{(+)*} + M_{12}^{(+)}] + \Omega_{R20}^2[L_2^{(+)*} + L_1^{(+)}] + i(\Delta_R + k_{12}v)\}\rho_{12}^{(+)}$$

$$+\Omega_{R20}^2 L_1^{(+)}e^{i\theta}\rho_{11}^{(0)} + \Omega_{R20}^2 L_2^{(+)*}e^{i\theta}\rho_{22}^{(0)} + \Omega_{R1}^2 M_{12}^{(+)}\rho_{11}^{(+)} + \Omega_{R1}^2 M_{21}^{(+)*}\rho_{22}^{(+)}$$

$$-\Omega_{R20}^2[L_2^{(+)*} + L_1^{(+)}]e^{i\theta}\rho_{33}^{(0)} - \Omega_{R1}^2[M_{21}^{(+)*} + M_{12}^{(+)}]\rho_{33}^{(+)} = 0, \tag{A7}$$

and, since $\rho_{21}^{(-)} = \rho_{12}^{(+)*}$, we have

$$\{G + \Omega_{R1}^2[M_{21}^{(+)} + M_{12}^{(+)*}] + \Omega_{R20}^2[L_2^{(+)} + L_1^{(+)*}] - i(\Delta_R + k_{12}v)\}\rho_{21}^{(-)}$$

$$+\Omega_{R20}^2 L_1^{(+)*}e^{-i\theta}\rho_{11}^{(0)} + \Omega_{R20}^2 L_2^{(+)}e^{-i\theta}\rho_{22}^{(0)} + \Omega_{R1}^2 M_{12}^{(+)*}\rho_{11}^{(-)} + \Omega_{R1}^2 M_{21}^{(+)}\rho_{22}^{(-)}$$

$$-\Omega_{R20}^2[L_2^{(+)} + L_1^{(+)*}]e^{-i\theta}\rho_{33}^{(0)} - \Omega_{R1}^2[M_{21}^{(+)} + M_{12}^{(+)*}]\rho_{33}^{(-)} = 0. \tag{A8}$$

Analogously, for $\rho_{12}^{(-)}$ and $\rho_{21}^{(+)} = \rho_{12}^{(-)*}$ we can derive the following

$$\{G + \Omega_{R1}^2[L_2^{(-)*} + L_1^{(-)}] + \Omega_{R20}^2[M_{21}^{(-)*} + M_{12}^{(-)}] + i(\Delta_R - k_{12}v)\}\rho_{12}^{(-)}$$

$$+\Omega_{R20}^2 M_{21}^{(-)*}e^{i\theta}\rho_{22}^{(0)} + \Omega_{R20}^2 M_{12}^{(-)}e^{i\theta}\rho_{11}^{(-)} + \Omega_{R1}^2 L_1^{(-)}\rho_{11}^{(0)} + \Omega_{R1}^2 L_2^{(-)*}\rho_{22}^{(0)}$$

$$-\Omega_{R20}^2[M_{21}^{(-)*} + M_{12}^{(-)}]e^{i\theta}\rho_{33}^{(-)} - \Omega_{R1}^2[L_2^{(-)*} + L_1^{(-)}]\rho_{33}^{(0)} = 0, \tag{A9}$$

$$\{G + \Omega_{R1}^2[L_2^{(-)} + L_1^{(-)*}] + \Omega_{R20}^2[M_{21}^{(-)} + M_{12}^{(-)*}] - i(\Delta_R - k_{12}v)\}\rho_{21}^{(+)}$$

$$+\Omega_{R20}^2 M_{21}^{(-)}e^{-i\theta}\rho_{22}^{(+)} + \Omega_{R20}^2 M_{12}^{(-)*}e^{-i\theta}\rho_{11}^{(+)} + \Omega_{R1}^2 L_1^{(-)*}\rho_{11}^{(0)} + \Omega_{R1}^2 L_2^{(-)}\rho_{22}^{(0)}$$

$$-\Omega_{R20}^2[M_{21}^{(-)} + M_{12}^{(-)*}]e^{-i\theta}\rho_{33}^{(+)} - \Omega_{R1}^2[L_2^{(-)} + L_1^{(-)*}]\rho_{33}^{(0)} = 0. \tag{A10}$$

In these equations, the two-photon (Raman) detuning $\Delta_R = \omega_1 - \omega_2 - \Omega_g$ and absolute value of the Rabi frequency $\Omega_{R20} = |\Omega_{R2}|$ have been introduced. The following notations for saturation parameters (S) and complex Lorentzian (L and M) have been also exploited

$$S_{mn}^{\pm} = \frac{|\Omega_{Rn}|^2}{\Gamma_{eg}^2 + (\omega_m - \omega_{3m} \pm k_m v)^2}, \qquad L_m^{\pm} = \frac{1}{\Gamma_{eg} + i(\omega_m - \omega_{3m} \pm k_m v)},$$

$$M_{mn}^{\pm} = \frac{1}{\Gamma_{eg} + i(\omega_m - \omega_{3m} \pm [k_m - 2k_n]v)}. \tag{A11}$$

It is also convenient to replace $\omega_1 - \omega_{31} = \Delta + \Delta_R/2$ and $\omega_2 - \omega_{32} = \Delta - \Delta_R/2$ with Δ, the one-photon detuning from the state $|3\rangle$, which has been scanned in the experiments to observe the absorption profiles.

Instead of the analogous equations for the spatial harmonics of excited-state population ρ_{33} (which are pretty long), the following common equation can be derived by summing the equations for the populations of all states ρ_{33}, ρ_{22} and ρ_{11} from (2)

$$\left(\frac{\partial}{\partial t} + v\frac{\partial}{\partial z} + G\right)[\rho_{11} + \rho_{22} + \rho_{33}] + 2\Gamma(1 - \beta)\rho_{33} = G. \tag{A12}$$

In particular, for zero spatial harmonics, we get

$$\rho_{11}^{(0)} + \rho_{22}^{(0)} + \rho_{33}^{(0)} = 1 - 2\Gamma\tau(1 - \beta)\rho_{33}^{(0)} \tag{A13}$$

with $\tau \equiv G^{-1}$. This equation has a very clear sense. In the case of an open system of atomic energy levels ($\beta < 1$), the full track of the density matrix $\widehat{\rho}^{(0)}$ over a time τ decreases by the value $2\Gamma(1 - \beta)\rho_{33}^{(0)} \times \tau$. For a closed system of levels ($\beta = 1$), we have the obvious expression $\text{Tr}[\widehat{\rho}^{(0)}] = 1$. For the other harmonics, equations are also very simple

$$(G - 2\mathrm{i}k_{12}v)[\rho_{11}^{(-)} + \rho_{22}^{(-)} + \rho_{33}^{(-)}] + 2\Gamma(1 - \beta)\rho_{33}^{(-)} = 0, \tag{A14}$$

and

$$(G + 2\mathrm{i}k_{12}v)[\rho_{11}^{(+)} + \rho_{22}^{(+)} + \rho_{33}^{(+)}] + 2\Gamma(1 - \beta)\rho_{33}^{(+)} = 0, \tag{A15}$$

Finally, the system of equations (A1)–(A15) can be written in the vector form

$$\widehat{\mathcal{L}}\boldsymbol{\rho} = \mathbf{C}_0, \tag{A16}$$

where we introduce the vector

$$\boldsymbol{\rho} = \{\rho_{11}^{(0)},\ \rho_{22}^{(0)},\ \rho_{33}^{(0)},\ \rho_{11}^{(-)},\ \rho_{22}^{(-)},\ \rho_{33}^{(-)},\ \rho_{12}^{(-)},\ldots,\rho_{21}^{(+)}\}^{\mathrm{T}}. \tag{A17}$$

The vector $\mathbf{C}_0$ has a simple structure

$$\mathbf{C}_0 = \{G/2,\ G/2,\ G,\ 0,\ldots,0\}^{\mathrm{T}}, \tag{A18}$$

and the matrix elements of the Liouvillian $\widehat{\mathcal{L}}$ can be defined from the explicit forms of the equations written above. Then the solution of the system is $\boldsymbol{\rho} = \widehat{\mathcal{L}}^{-1}\mathbf{C}_0$.

References

[1] Arimondo E, Inguscio M and Violino P 1977 *Rev. Mod. Phys.* **49** 1
[2] Ye J, Swartz S, Jungner P and Hall J L 1996 *Opt. Lett.* **21** 1280
[3] Demtroder W 2003 *Laser Spectroscopy: Basic Concepts and Instrumentation* 3rd edn (Berlin: Springer) section 5.4.5 (https://doi.org/10.1007/978-3-662-05155-9)
[4] Hansch T W, Schawlow A L and Series G W 1979 *Sci. Am.* **240** 94
[5] Chu S 1998 *Rev. Mod. Phys.* **70** 685
[6] Cohen-Tannoudji C 1998 *Rev. Mod. Phys.* **70** 707
[7] Philipps W D 1998 *Rev. Mod. Phys.* **70** 721
[8] Anderson M H, Ensher J R, Matthews M R, Wieman C E and Cornell E A 1995 *Science* **269** 198–201
[9] Letokhov V S 1976 Saturation spectroscopy *High Resolution Laser Spectroscopy* (*Topics in Applied Physics*) ed K Shimoda vol 13 (Berlin: Springer) 4
[10] Schawlow A L 1982 *Rev. Mod. Phys.* **54** 697–707
[11] Rovera G D, Santarelli G and Clairon A 1994 *Rev. Sci. Instrum.* **65** 1502–5
[12] Affolderbach C and Mileti G 2005 *Opt. Lasers Eng.* **43** 291–302
[13] Affolderbach C and Mileti G 2005 *Rev. Sci. Instrum.* **76** 073108
[14] Baillard X, Gauguet A, Bize S, Lemonde P, Laurent P, Clairon A and Rosenbusch P 2006 *Opt. Commun.* **266** 609–13
[15] Liu X and Boudot R 2012 *IEEE Trans. Instrum. Meas.* **61** 2852–5
[16] Liang W, Ilchenko V S, Eliyahu D, Dale E, Savchenkov A A, Seidel D, Matsko A B and Maleki L 2015 *Appl. Opt.* **54** 3353–9
[17] Kol'chenko A P, Rautian S G and Sokolovskii R I 1969 *J. Exp. Theor. Phys.* **28** 986
[18] Hall J L, Borde C J and Uehara K 1976 *Phys. Rev. Lett.* **37** 1339
[19] Bagaev S N, Dmitriev A K, Nekrasov Y V and Skvortsov B N 1989 *JETP Lett.* **50** 194
[20] Ishikawa J, Riehle F, Helmcke J and Borde C J 1994 *Phys. Rev.* A **49** 4794
[21] Vasil'ev V V, Velichanskii V L, Zibrov S A, Sivak A V, Brazhnikov D V, Taichenachev A V and Yudin V I 2011 *J. Exp. Theor. Phys.* **112** 770
[22] Pappas P G, Burns M M, Hinshelwood D D, Feld M S and Murnick D E 1980 *Phys. Rev.* A **21** 1955
[23] Schmidt O, Knaak K M, Wynands R and Meschede D 1994 *Appl. Phys.* B **59** 167
[24] McFerran J 2016 *J. Opt. Soc. Am.* B **33** 1278
[25] Lee H S, Park S E, Park J D and Cho H 1994 *J. Opt. Soc. Am.* **11** 558
[26] Brazhnikov D V, Novokreshchenov V K, Ignatovich S M, Taichenachev A V and Yudin V I 2016 *Quantum Electron.* **46** 453
[27] Lazebnyi D B, Brazhnikov D V, Taichenachev A V, Basalaev M Y and Yudin V I 2015 *J. Exp. Theor. Phys.* **121** 934
[28] Abdel Hafiz M, Coget G, De Clercq E and Boudot R 2016 *Opt. Lett.* **41** 2982
[29] Abdel Hafiz M, Liu X, Guérandel S, De Clercq E and Boudot R 2016 *J. Phys.: Conf. Ser.* **723** 012013
[30] Abdel Hafiz M and Boudot R 2015 *J. Appl. Phys.* **118** 124903
[31] Arimondo E 1996 *Prog. Opt.* **35** 257
[32] François B, Calosso C E, Danet J M and Boudot R 2014 *Rev. Sci. Instrum.* **85** 094709

[33] Liu X, Mérolla J M, Guérandel S, Gorecki C, De Clercq E and Boudot R 2013 *Phys. Rev.* A **87** 013416
[34] Smirnov V S, Tumaikin A M and Yudin V I 1989 *J. Exp. Theor. Phys.* **69** 913
[35] Brazhnikov D V, Taichenachev A V and Yudin V I 2011 *Eur. Phys. J.* D **63** 315
[36] Abdel Hafiz M, Coget G, Yun P, Guérandel S, de Clercq E and Boudot R 2017 *J. Appl. Phys.* **121** 104903
[37] Kargapoltsev S V, Kitching J, Hollberg L, Taichenachev A V, Velichansky V L and Yudin V I 2004 *Laser Phys. Lett.* **1** 495–9
[38] Brazhnikov D V, Taichenachev A V, Tumaikin A M, Yudin V I, Ryabtsev I I and Entin V M 2010 *JETP Lett.* **91** 625
[39] Bloch D, Ducloy M, Senkov N, Velichanskii V and Yudin V 1996 *Laser Phys.* **6** 670–8
[40] Kazakov G, Matisov B, Mazets I, Mileti G and Delporte J 2005 *Phys. Rev.* A **72** 063408
[41] Zibrov S A, Velichansky V L, Zibrov A S, Taichenachev A V and Yudin V I 2005 *JETP Lett.* **82** 477–81
[42] Kozlova O, Danet J M, Guérandel S and de Clercq E 2014 *IEEE Trans. Instrum. Meas.* **63** 1863
[43] Kosachev D V, Matisov B G and Rozhdestvensky Y V 1992 *J. Phys. B: At. Mol. Opt. Phys.* **25** 2473–88
[44] Taichenachev A V, Yudin V I, Velichansky V L and Zibrov S A 2005 *JETP Lett.* **82** 398–403
[45] Kazakov G A, Matisov B G, Mazets I E and Rozhdestvensky Y V 2006 *Tech. Phys.* **51** 1414–24